University of Zurich[UZH]

# Bachelor Thesis

# Characterisation of Silicon Photomultipliers for Xenoscope

Julian Haas
Morgenstrasse 12
8266 Steckborn
tel. 079 914 08 18
julianpaulrobert.haas@uzh.ch

Supervisor: Dr. Ricardo Peres

20th August 2023

# Contents

**Abstract**

To date, the nature of dark matter is still an open topic in modern physics. In the hypothesis that dark matter consists of particles, they are hoped to be observed in detectors on Earth. DARWIN is a planned detector using a dual-phase liquid xenon time projection chamber at the 50t scale. It aims to observe such particles, or to constrain the cross section of potential dark matter particles to the point where solar and atmospheric neutrinos will become background. This work first introduces the evidence and search for dark matter. It discusses Xenoscope, a DARWIN demonstrator built at the University of Zürich. For the instrumentation of DARWIN and Xenoscope, low noise photosensors are needed. The characterisation of a set of VUV4 S13371-6050CQ-02 MPPCs produced by Hamamatsu Photonics is presented in this work. These photosensors will be assembled into Xenoscope in an array, which is discussed here. The results obtained from this characterisation are a breakdown voltage of $(46.5 \pm 0.5)$V at 190 K, with a gain of $(3 \pm 0.2) \cdot 10^6$ at a bias voltage of 52V and a temperature of 190 K. This gain is a substantial increase from the previous model [1]. At this gain and temperature, the crosstalk probability was measured to be $(15 \pm 1)\%$. The dark count rate of $\mathcal{O}(\mathrm{Hz/mm^2})$ is still considerably higher than for PMT candidates [1].

# 1 Introduction to dark matter searches

There is strong evidence that the matter that makes up our bodies, planets and stars, might only be a small fraction of the total matter in the Universe. Dark Matter (DM) is a concept that states that much of the mass in our Universe belongs to a different kind of matter to what is known to us. It is not visible and presumably interacts very rarely with particles in the Standard Model (SM). Yet, its gravitational effects are observed throughout the Universe.
Over the last century, the effort for explaining and detecting DM has become one of the most central interests of astrophysics and astroparticle physics. The evidence for its existence is plentiful and the effects of DM can be observed at many different size scales, fundamentally influencing the shape and nature of our Universe. In the following sections, the most striking evidence for the existence of DM, as well as theorised particle candidates, are briefly discussed. Furthermore, an insight into detection experiments and the development towards the DARWIN observatory, is given. The main part of this work focuses on the characterisation of Silicon Photomultipliers (SiPMs), and discussing their usability as photosensors in Xenoscope, a DARWIN demonstrator being developed by the Astroparticle Physics Group of the University of Zurich.

## 1.1 Cosmological evidence

### 1.1.1 Galactic scales

The most striking evidence for the existence of DM arises from the gravitational influence on the rotational velocity of stars within a galaxy. From Newtonian dynamics, the velocity distribution is to follow the relation

$$v(r) = \sqrt{\frac{GM(r)}{r}}, \tag{1}$$

where

$$M(r) \equiv 4\pi \int \rho(r) r^2 \, \mathrm{d}r, \tag{2}$$

with $\rho(r)$ being the mass density of a galaxy, r being the distance of the star to the centre of the galaxy, and G the Gravitational constant. The overwhelming amount of visible matter we see in galaxies is located around the centre of the galaxy. Thus, only little dependence of $M(r)$ to $r$ is expected and the velocity is expected to follow $v(r) \propto 1/\sqrt{r}$. Instead, one observes that v(r) is close to constant, which implies $M(r) \propto r$ and thus $\rho(r) \propto 1/r^2$. To match this difference in luminous intensity seen from the galaxy and the movement of its stars, a model was introduced which includes a halo of matter which does not interact with light, and whose mass accounts for

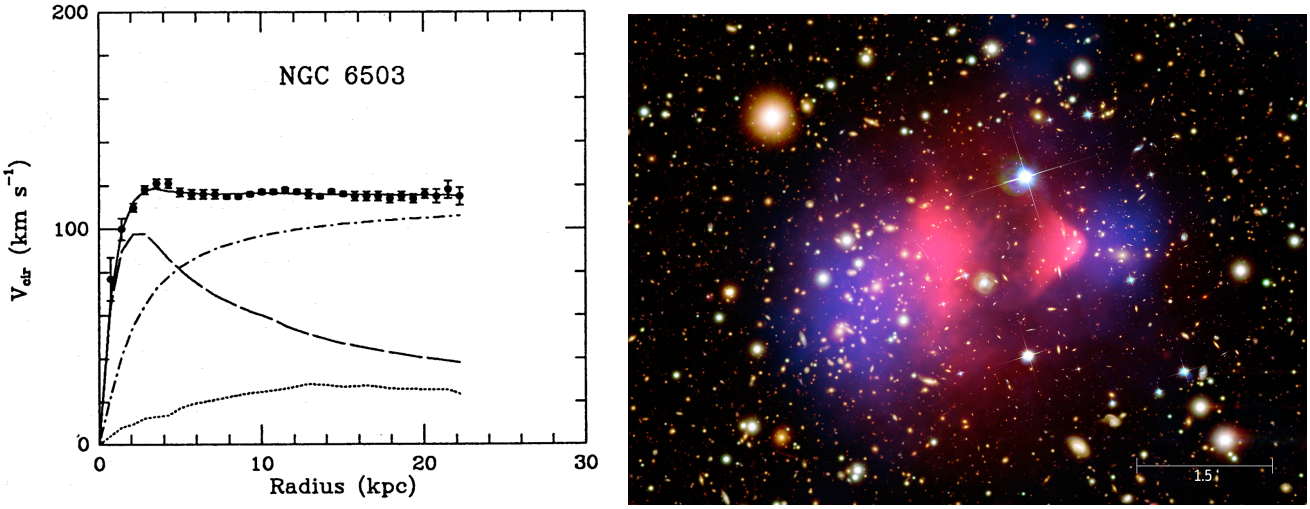


***Figure 1:*** *(Left): Rotation curves for the galaxy NGC 6503. The dashed lines show the expected curve due to luminous matter, the dotted line for the gas, and the dash-dotted line for the dark matter halo. The sum of these three components agrees well with recorded data. Figure from [2]. (Right): Image of the Bullet galaxy cluster. Coloured pink is the x-ray emission of intergalactic gas clouds. Coloured blue is the mass distribution calculated by Chandra by observing gravitational lensing effects [3]. Figure from NASA/CXC/SAO.*

the flat distribution of rotational velocities, as seen in fig. 1.

### 1.1.2 Intergalactic scale

Already predicted by the theory of General Relativity, light is also attracted by gravity and thus can bend in the presence of a gravitational field. This effect was observed during solar eclipses, where the position of stars behind the Sun did non exactly line up with expectations[4]. On a larger (and for this work more important) scale, we observe gravitational lensing. There, the light of a whole galaxy is bent by the gravitational field of another galaxy located in front of it. The distorted image, which shows differences to what is expected by the mass of the galaxy in the centre, when only the luminous components are considered. A halo of non visible matter could explain the discrepancy in this case as well [5].

A more recent and strong argument for the existence of DM is the image of the Bullet galaxy cluster, taken by the Chandra X-ray observatory (see fig. 1). The observed centre of mass of these two colliding galaxy clusters, determined by studying the effects of gravitational lensing in

the image, is different by over 8 $\sigma$ from the predicted centre of mass considering only luminous intensity form x-ray emissions by the intergalactic gas clouds[3].

### 1.1.3 Universal, non-local evidence

Whilst the evidence for dark matter discussed so far appears to be consistent at different scales, it does only show its effects on a local scale, and does not quantify how much DM there is in relation to luminous, baryonic matter.
Research in this field began fundamentally in the second half of the 20th century with the discovery of the Cosmic Microwave Background (CMB) in 1964, leading to general agreement in the Big Bang hypothesis, which states that the Universe expanded from a singularity of high density and temperature. This model provides an explanation for the continuous expansion of the Universe, the distribution of light elements across the Universe, as well as the small differences (anisotropies) in the temperature readings of the CMB, depending on which direction the temperature was measured. The current temperature of 2.725 K is what remains of the high temperature of the Universe in the first few thousand years after the big bang. The anisotropies, explained as quantum fluctuations (now scaled up to the size of the Universe today), are a prime factor why pure-baryonic (no dark matter or dark energy) models of the Universe had to be discarded. A second model saw the Universe as a mixture of dark matter and light matter, which better predicted the formation of galaxies and galaxy clusters, but required an expansion of the Universe lower than observed [6]. After the discovery of the accelerated expansion of the Universe in 1998, a third model called the $\Lambda CDM$ model, was postulated and provides the best explanation for the formation of large scale structures like galaxy filaments and cosmic voids, incorporating dark matter, as well as dark energy [6]. Over the years, precise studies of the CMB have been conducted. The Planck satellite currently provides the most accurate composition of the Universe, with 4% baryonic matter, 27% dark matter, and 69% dark energy [7].

Despite making up over a quarter of the matter and energy density of our Universe, little is known about DM, and it has not been directly detected so far. DM could be composed of one or more particles. Extensive research is being conducted to directly detect it by searching for its interactions with baryonic targets.

## 1.2 Particle candidates

The effects attributed to DM could be explained by alternative theories which do not involve adding new particles to the Standard Model. They explain the effects of DM by modifying our current understanding of gravitational laws, such as MOND [8], and have even been expanded for relativistic effects (TeVeS) [9]. The modifications however cannot predict all the discussed phenomena simultaneously.
Similarly, one could argue that the observations from the luminous intensity of the galaxies could be incomplete, as they do not account for massive baryonic, but non luminous objects, like planets, black holes and others, jointly referred to as MACHO's (Massive Compact Halo Objects). However experiments like MACHO [10] and EROS [11] have concluded that MACHOs could account for no more than a fifth of the observed dark matter.

Looking into particle candidates for dark matter, a logical first step is to start with the already known and observed particles of the Standard Model. From all the particles in the SM, only one is a realistic DM candidate, the neutrino. The neutrino is neutral and has very low interaction rates with other SM particles. Combining the information provided by CMB and direct neutrino observations (solar and atmospheric), their mass is not sufficient to explain the DM content. Therefore, we focus on new proposed particles and their potential detection.

One prime candidate is the axion, which was initially proposed after 1970 as a possible explanation to the *strong CP problem*. CP violation has been observed in certain weak interactions, but never at the Quantum Chromodynamic (QCD) level [12]. Nonetheless, there is no reason why CP symmetry should be conserved only in QCD. The axion, although not yet observed, is a prime candidate for dark matter, with numerous experiments built, trying to detect it [13, 14, 15].
Another well known theory is Supersymmetry, where Standard Model particles are assigned partner particles with different masses and opposite spin, which provided DM candidates such as the *gravitino* or the *neutralino* [16]. No experimental evidence supports so far the existence of Supersymmetry.
This lack of evidence has led scientists to look for dark matter particles in a more broad spectrum. Experiments such as XENON[17], LZ[18], PandaX[19] and, in the future, DARWIN[20] have been designed to look for a wide range of particle masses, trying to observe the rare interactions these DM candidates could have with atomic nuclei and electrons. Properties and detection methods of these Weakly Interactive Massive Particles (WIMPs) shall be discussed in the following section.

### 1.2.1 The WIMP

Seeing that the effects of dark matter can be observed today and in previous stages of the Universe by observing more distant galaxies, one can conclude that the relic density of DM in the Universe has remained constant for most of the Universes lifetime. The reason the DM density has arrived to this low and constant value is believed to be explained by the temperature of the Universe right after the Big Bang [21]. For temperatures $T >> m_\chi$, the mass of the DM WIMPs, its equilibrium abundance is equal to that of photons [21]. Only when the temperature of the Universe decreases below the dark matter WIMP mass, we have more annihilation of WIMPs than creation, proportional to $e^{-m_x/T}$ (see fig. 2), until it "freezes out" [21]. The previously discussed DM candidates do also fall under the WIMP definition. There are currently no Standard Model candidates for WIMPs.

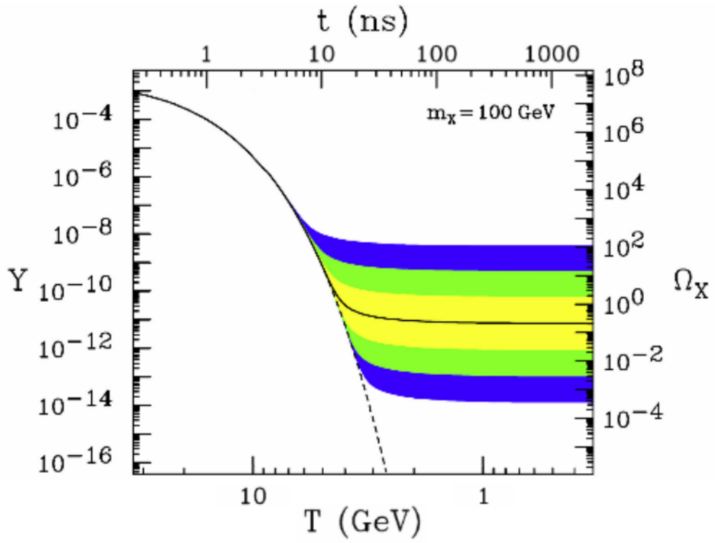


***Figure 2:*** *Dark matter density (left axis), and resulting thermal relic density (right axis) for a 100 GeV WIMP particle as function of temperature (bottom) and time (top). The solid line shows the DM density becoming constant for increasing temperature (compared to the dashed line for particles that would remain in thermal equilibrium) at the observed relic density of DM. Shaded regions differ from this value by 10,* $10^2$ *and* $10^3$*. Figure from [22].*

### 1.2.2 Direct detection techniques

Currently, there are three different approaches to look for DM: production at colliders, indirect detection by detecting reaction products, and direct detection. Each uses different types of ex-

periments. In production by collision, two standard matter particles are collided such that the collision energy is sufficient to produce WIMPs. The created WIMPs cannot be detected, but if the summed up energies of the interaction products differs from the summed up energies of the reaction partners, the missing energy could belong to a WIMP. In recent years, the ATLAS [23] and CMS [24] experiments at the Large Hadron Collider at CERN have conducted searches for WIMPs, finding so far no evidence.[25]
Indirect detection focuses not on the detection of DM particles themselves, but instead on DM-DM interaction products, which are expected to be SM particle pairs, like $\gamma\gamma, \gamma Z, \gamma H, q\bar{q}$, among others [26]. As DM exerts gravity, it is assumed to be locally more abundant in regions of high matter density, such as galactic centres or stars. Thus, it is expected that there will be more DM-DM interactions in these regions, and therefore more reaction products are expected from these directions. However, there are many other sources for the same possible reaction products, which could make their attribution to DM problematic [27]. Experiments for indirect detection include the FERMI-LAT satellite [28], the AMS-02 experiment on the ISS [29], or IceCube in Antarctica [30].

As the name suggests, direct detection experiments aim to directly observe a DM particle interacting with standard matter here on Earth. This interaction is in the form of a DM particle scattering coherently with a whole nucleus, or in a spin-dependent interaction with only one nucleon (proton or neutron) of a nucleus. In broad terms, detector designs can be attributed to one of four types:

- *Bubble chambers* are being used for direct detection experiments, aiming to detect a DM particle scattering with the superheated liquid, triggering a phase transition which might release charged particles which leave bubble trails. One of these experiments is PICO at SNOLAB in Canada [31].

- *Cryogenic crystal detectors*, where disks of certain semiconducting crystals are cooled. A DM particle scattering on the crystal lattice would transfer enough energy to the lattice, such that its temperature changes enough that attached superconducting thermal sensors detect it. CRESST at the Laboratori Nazionali del Gran Sasso (LNGS) works with this principle [32].

- *Crystal scintillators* also use crystals, but their scintillating properties are used, as the scintillation light emitted when a DM particle scatters off the crystal. This light can in turn be detected by a photomultiplier. One of the crystal scintillators is the DAMA/LIBRA experiment at LNGS, which has published results claiming to have detected a change in the interaction rate measured. The change is attributed to the rotation of the Earth around the Sun. In the course of a year, the Earths rotation around the sun is once opposite the rotation of the Milky Way, and once in the same direction. The change in interaction rate would thus be explained by the change of flux of DM particles the Earth gets over the course of one year due to modulating rotational velocities around the galactic centre[33]. On the other hand, similar experiments around the world have so far failed to confirm these results [34].

- *Liquid noble gas time projection chambers (TPC)* detect the scintillation and charge released in the interaction from a DM particle with the target atom. The emitted photons are detected by photosensors, while the released charge is drifted with the use of an electric field and detected as a secondary proportional scintillation signal. The techniques of these detectors will be discussed extensively in section 2. LZ and XENONnT are two running experiments using this method [18, 17]. DARWIN is a planned experiment with even higher sensitivity [20].

# 2 Xenoscope, a full scale vertical Demonstrator for DARWIN

## 2.1 The Dual-Phase LXe Time Projection Chamber

Dual-phase LXe TPCs are being used in many current direct detection experiments, such as XENONnT [17], LUX-ZEPLIN [18], and PandaX-4T [19], and DARWIN is set to follow this trend.

The detection of particles using this setup starts with scintillation in LXe. A particle can interact with a xenon atom leading to nuclear recoil (NR) or electronic recoil (ER) and both ionises and excite the atom: The excited atom can combine with a second xenon atom to form a $Xe_2$ molecule in an excimer state. In the de-excitation, the dimer returns to two xenon atoms, and in this process a characteristic 178 nm photon is released [35]. These 178 nm photons in turn do not excite xenon atoms, which allows them to propagate through the xenon. The emitted photons can be detected by the photosensor array on the top or bottom of the chamber. The side walls are designed in such a way that the photons can be very well reflected, in order to maximise the detection of the photons in the TPC. The first prompt signal from these photons is called S1. The number of detected photons scales with the number of released ionisation electrons, which in turn scales with the recoil energy and detection performance.

The interaction with xenon atoms also produces free charges released from the atoms. These electrons then find themselves in an electric field ($E_{drift}$). The electron cloud drifts upwards until it passes the gate, a grounded stainless steel mesh, where it experiences an even stronger electric field ($E_{extraction}$) between gate and the anode mesh. Between the gate and the anode, the electrons traverse the liquid-gas interface. $E_{extraction}$ induces further scintillation, where again 178 nm photons are emitted and detected as the secondary signal called S2.

Even when reflected, the photons are fast enough to be detected nearly instantly, and the time difference between the S1 and S2 signal is solely dependant on the time the electrons take to drift. In turn, this depends on the strength of the electric field and the position in the chamber where the recoil happened (denoted as drift time in fig. 3). The position reconstruction is based on the time difference thus allows us to directly calculate the Z coordinate of the recoil. The X and Y coordinates are found by the pattern produced by the photosensors of the top array detecting the S2 signal. As this signal is created in the narrow GXe phase, the sensors are close enough to cover a sufficient altitude angle such that the origin of the signal can be estimated based on the hit pattern (see fig. 3).

Depending on whether the signals come from ER or NR, the detected signal varies in width and amplitude, most prominently the S2 signal. Thus, by comparing the sizes of S1 and S2, it can be

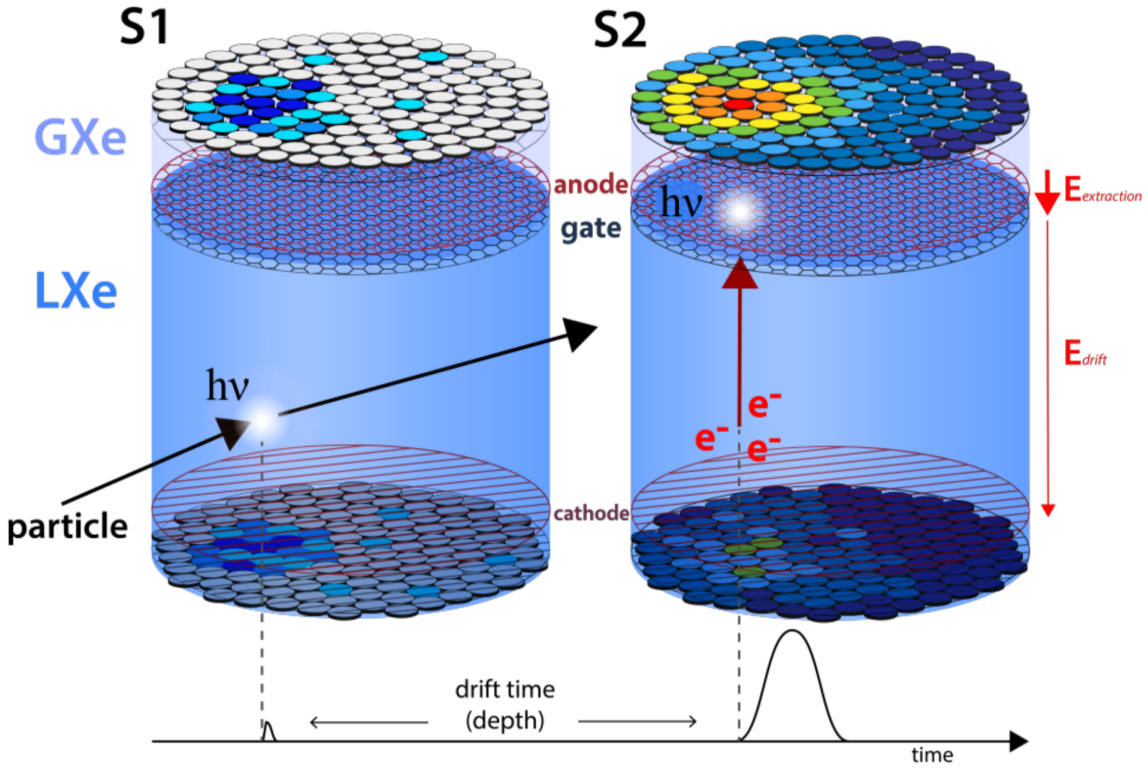


***Figure 3:*** *Schematic of the dual phase TPC working principle. Figure from [22]*

determined whether the detected interaction was ER or NR.

In the cases of higher energy recoils, the signal can saturate, which is why further data analysis tools are needed to estimate energies above 200keV [36].

## 2.2 The DARWIN project

DARk matter WImp search with liquid xenoN (DARWIN) will be a future observatory, with a total of 50 tons of LXe target acting as a scintillator. DARWIN will be the next generation of xenon based TPCs, such as XENONnT and LZ. The XENON collaboration has since 2002 been developing dual phase TPCs of ever increasing size. XENON10 (2006) with a target of 14 kg of LXe, XENON100 (2008) with 62 kg, XENON1T (2016) with 2 tons, and most recently XENONnT with 5.9 tons, which is currently taking data [37]. DARWIN is set to be the final iteration of these LXe DM detectors. The increase in LXe volume has resulted in increasingly smaller lower bounds

for spin-independent WIMP-nucleus (SI) and spin-dependent (SD) WIMP-neucleon interaction cross sections. DARWIN is hoped to decrease this lower bound by about an order of magnitude from XENONnT for WIMP masses above 5 GeV/$c^2$ [20] (see fig. 4).

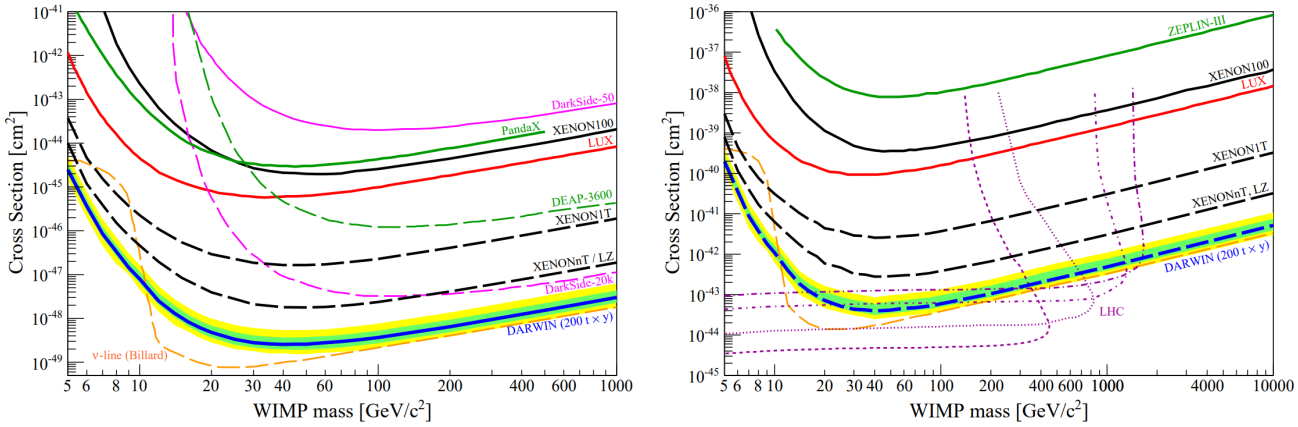


***Figure 4:*** *Expected sensitivity for spin-independent (left) and spin-dependent (right) WIMP-nucleon cross sections for DARWIN compared to other detectors. The ν-line denotes the irreducible neutrino background. Figure from[20].*

For cross sections in the order of $10^{-49}$cm$^2$ it is crucially important to further reduce any background sources as much as possible, which is why several steps towards shielding against background radiation have been taken. The most important background sources for DARWIN are cosmogenic and radiogenic neutrons, intrinsic backgrounds of the target materials, and neutrino induced backgrounds. DARWIN is planned to be constructed in the underground facilities of LNGS, located below 1400 m of rock, which is an equivalent of 3400 m of water shielding. This provides excellent shielding against cosmic rays. An active Cherenkov muon veto in a 12 m diameter water tank will reduce the rate of cosmogenic neutrons to negligible levels [20]. Sophisticated purification techniques will allow levels of $^{\text{nat}}$Kr and $^{220}$Rn to be reduced below necessary thresholds for WIMP studies.

The neutrino flux cannot be shielded against going underground. Neutrino-nucleus and neutrino-electron scattering will lead to an irreducible background (orange line in fig. 4), below which the neutrino scatterings will dominate the recoil spectrum [20]. DARWIN is designed to reach a sensitivity right up to this limit.

## 2.3 Xenoscope

Xenoscope is an experiment designed and built at the University of Zürich. In its final configuration, its inner detector is a dual phase LXe TPC with a height of 2.6 m (see fig. 5), the same height as the DARWIN baseline scenario. The main purpose of this facility is to demonstrate the drift of electrons by an applied electric field, created by a lamp shining on a photocathode at the bottom, over the whole distance of 2.6 m. The challenge is to transport electrons through LXe, which therefore must be pure enough that they do not attach to impurities before they reach the top of the detector. An elaborate purification system aims to decrease the number of electronegative impurities in the LXe. The xenon is recirculated through this system in the gaseous phase, where a large flow and high efficiency is key. Xenoscope aims to achieve a drift field of $\sim 200$ V/cm and

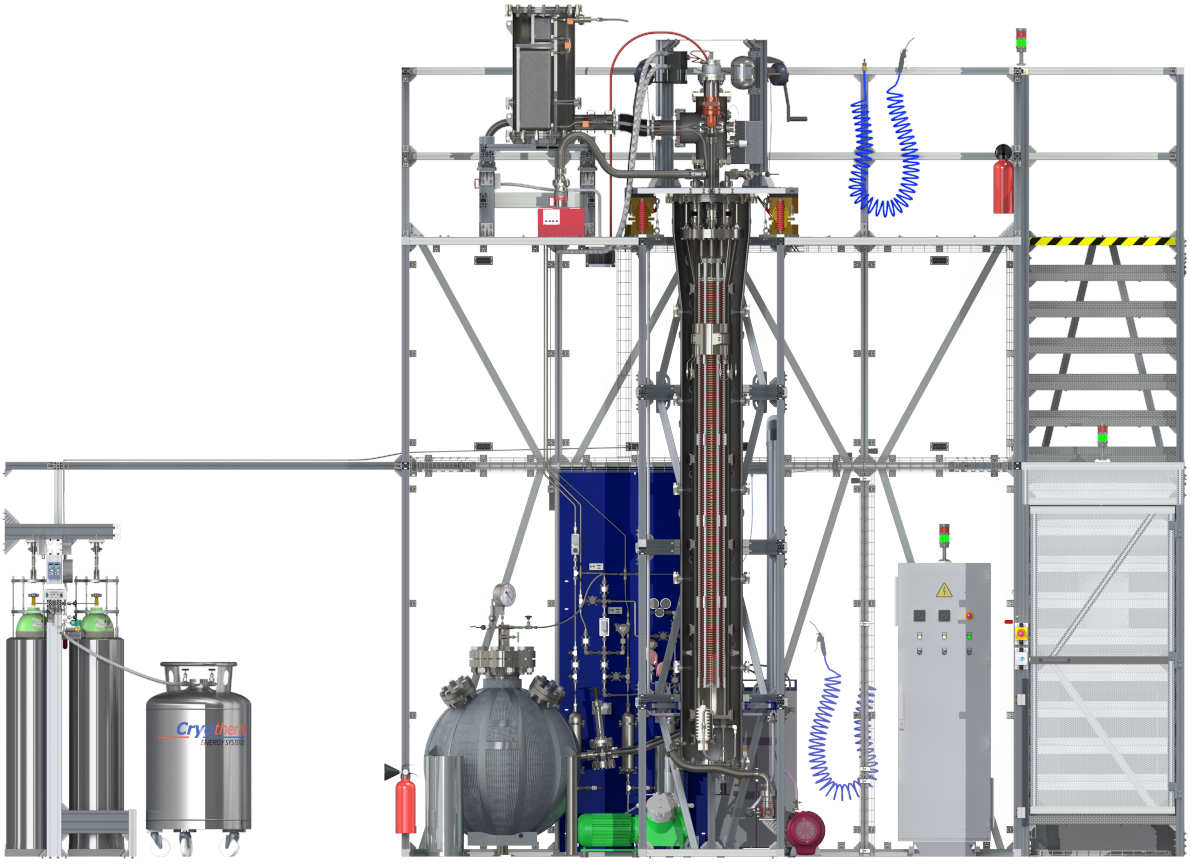


***Figure 5:*** *Render of Xenoscope, a DARWIN demonstrator built at Irchel Campus at UZH. Figure from [38].*

a gas recirculation flow of 70 slpm [39]. A high voltage in the LXe is crucial, as it decreases the drift time of the electrons. The purity of the xenon can be quantified by calculating the electron lifetime. The electron lifetime corresponds to the time at which an initial charge population decreases by a factor $e$, as it attaches to the electronegative impurities diffused in LXe. Achieving a high purity of the LXe will be obsered by a high electron lifetime.

In order to fulfil Xenoscope's main purpose of observing a full distance electron drift, a xenon lamp generates photons, which hit a photocathode at the bottom of the TPC, causing electrons to be released through photoelectric effect, which then drift through the chamber. A grid of SiPMs was designed to be installed at the top of the TPC to detect the photons created by these electrons extracted to the GXe phase. In the following sections, the design of this top array and the working principle of Silicon Photomultipliers is discussed, before presenting the setup and results of their characterisation campaign conducted for this work.

Working towards achieving a full 2.6m drift, the project is split into two phases. First, a purity monitor was instrumented in the LXe, with a drift length of 525 mm, for an initial measurement of electron lifetime. In its second phase this drift distance is increased to the full 2.6 m [39]. In the TPC phases of the project, the electrons are extracted into the gas phase, and a set of photosensors at the top of the TPC will detect the created photons from the scintillation.

In future experiments, Xenoscope aims to benchmark further important parameters for DARWIN, such as electron transport properties, drift speed, the Rayleigh scattering length and index of refraction of xenon, and will be used for testing subsystems, such as the SiPMs in this work.

# 3 Characterisation of SiPMs for the Xenoscope top array

For the main experimental part of this work, a set of Silicon Photomultipliers has been characterised to asses their usability as units in the photosensor array at the top of Xenoscope, to detect the S2 signals (as discussed in section 2.2). First, a brief overview of the physics behind SiPMs is given and the Xenoscope top array is presented. Next, the testing setup for the experiments is discussed before presenting the characterisation techniques and their results.

## 3.1 The SiPM working principle

A Silicon Photomultiplier is a multi-pixel photon counter (MPPC) which consists of a matrix of avalanche photodiodes (APD) connected in parallel. The size of one matrix and one APD (pixel) depends on the model. In this work, the model tested is a VUV4 S13371-6050CQ-02 MPPC, produced by Hamamatsu Photonics.

The APD is based on a positive intrinsic negative diode (PIN diode), which are p-n diodes, where the p-n junction is separated by an undoped intrinsic semiconductor region i. In an APD, this i region is now separated from the n region by another p region, making the APD technically a PIPN photodiode. The reason for adding this p region lies in the space charge distribution, which in this region is very high, with the electric field rising to a maximum right at the pn-junction.
The APD can thus be divided into two regions: The absoption region (i) and the multiplication region (pn-junction). Typically the i region is much larger, to cover the largest amount of space to detect more photons. A photon hits the absobtion region and creates an electron-hole pair via the photoelectric effect. Due to the applied voltage, the hole drifts to the p region, whilst the photoelectron drifts towards the multiplication region. Inside the i region, the electric field strength is small and increases only slightly when moving closer to the pn-junction. Once it reaches the highly doped p region, the field increases drastically, accelerating the electrons towards the n region. The electron does impact ionisation with the semiconductor material, where the valence electrons are elevated into the conduction band. The electron loses energy in the impacts, so if the electrons initial energy was not sufficient, it will recombine and itself fall into the valence band. As the energy of the electrons at the point of the impact is defined by their velocity caused by the electric field, the voltage at which the APD is operated, determines whether the electron still remains in the conduction band. If the voltage is high enough, each impact releases one additional electron into the conduction band, which itself can again do impact ionisation. This process in which the number of electrons increases exponentially (see fig. 6) is called avalanche breakdown.

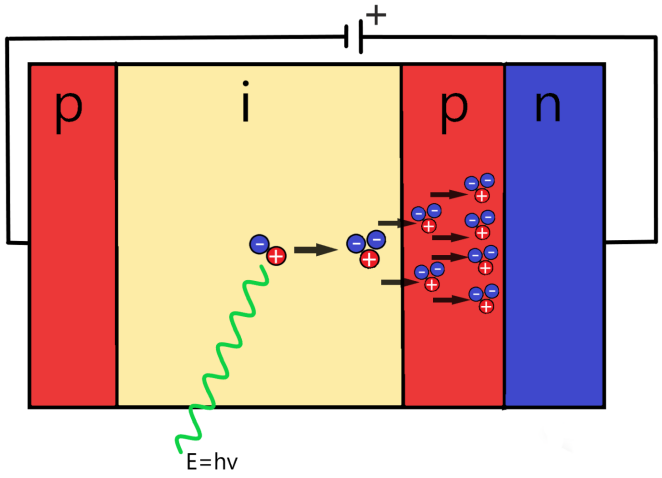


***Figure 6:*** *Schematic of the APD working principle. A photon leads to the release an electron via the photoelectric effect which then causes an avalanche by impact ionisation.*

The number of electrons released in the whole avalanche is called the gain of the avalanche. This gain can be saturated, and thus increasing the voltage would not result in increased gain. When all the present valence electrons are released into the conduction band, an APD operated at such a voltage is called Geiger-mode. The lowest possible voltage for Geiger-mode operation is called breakdown voltage (BV). This can now be further extrapolated to the SiPM as a whole, with the single APDs connected in parallel. The SiPM characterised in this work has quadratic APDs with a side length of 50 $\mu$m. A microscope view of the APD pixels of the tested SiPMs is seen in fig. 7. The BV and gain will be two of the main characteristics investigated in this work.

## 3.2 The Xenoscope top array

In order to detect the S2 signal in Xenoscope at the top of the TPC, an array of SiPMs has been designed. It is set to hold 192 single 6 $\times$ 6 mm$^2$ detectors, which Hamamatsu delivers in a 2 $\times$ 2 package. These 48 2 $\times$ 2s are now arranged in 12 tiles, with each tile holding four 2 $\times$ 2s (so 4 $\times$ 4 detectors). The readout comes from a summing circuit through a printed circuit board, with an incorporated low-noise OPA847 operational amplifier in a 20-fold pre-amplifier circuit, produced in house and based on a design by Arneodo et al [40]. Each tile has 5 power cables, three for the pre-amplifier and two for the SiPMs. Additionally, there is one signal cable for the readout. With this design of only twelve pre-amplifiers, the total number of cables is 72. For the characterisation,

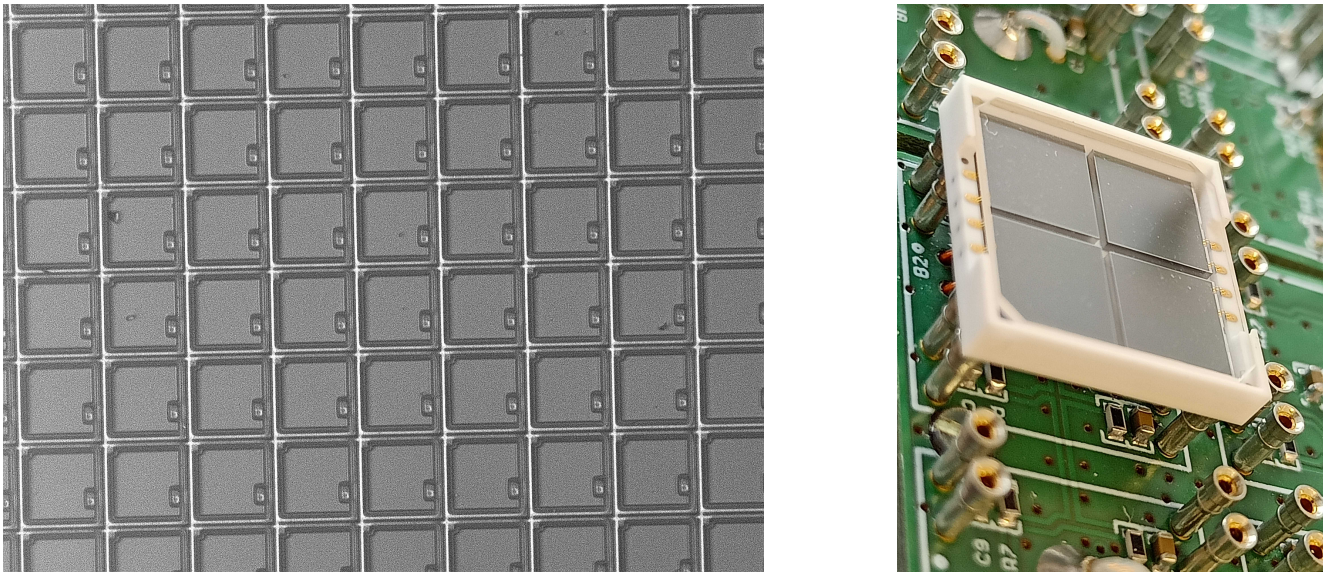

***Figure 7:*** *(left) 20× Microscope image of the quadratic APDs in the SiPM. Each square has a length of 50 µm. (right) A SiPM mounted on a PCB in the top array.*

each 2 × 2 SiPM needs to be evaluated separately to determine its specific properties. As the tile readout has a summing architecture, the testing is conducted in multiple runs, where a single tile holds only one of the four possible 12 × 12 $mm^2$ MPPCs. This way, each module readout only corresponds to data from one 2 × 2. Fig. 7 shows a 2 × 2 SiPM mounted on a 4 × 4 amplifier. The spacial resolution of a signal is limited by the covered space of all the tiles connected to one pre-amplifier. Still, the spacial resolution can be better than the tile size when the whole pattern of tiles is observed. As seen in fig. 8, the spaces between the tiles and modules will be covered by a Polytetrafluoroethylene (PTFE) cover. To save time, the characterisation of the SiPMs is combined with testing of the pre-amplifiers and the signal- and voltage-cables.

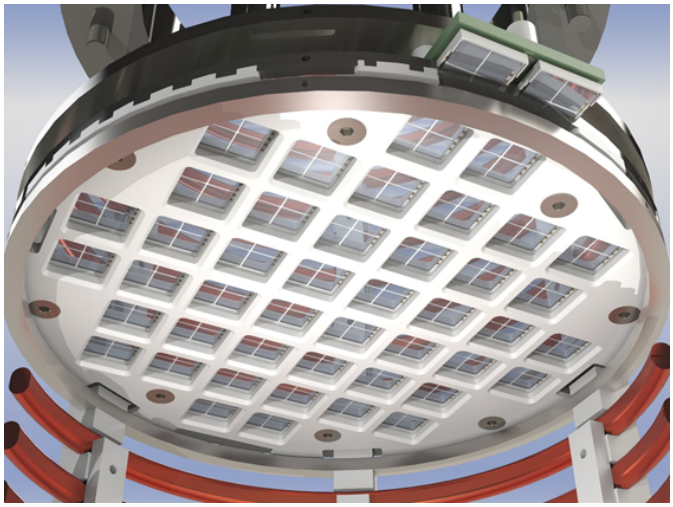

***Figure 8:*** *A rendered image of the top array mounted in Xenoscope. The SiPMs are exposed through cutouts in the PTFE cover. They are arranged to cover as much of the area as possible.*

## 3.3 Testing with the Liquid Argon Setup

### 3.3.1 Description of the setup

The Liquid Argon Setup (LArS) is a testing facility in the H-floor lab of the Institute of Physics in Zurich. LArS was first designed to test wavelength shifters for the GERDA experiment (LArS-I), but has since been updated and repurposed as a general photosensor testing facility (LArS-II). LArS provides a temperature and pressure controlled dark space, which can be filled with a preferred gas. This provides a suitable environment for the SiPM testing.

The core piece of LArS is the inner cell (see fig. 9), mounted on a frame. It is a cylindrical vacuum chamber, with the top flange connected to the bottom part via a set of screws. A rubber O-ring ensures that pressures in the order of a few $10^{-4}$ mbar can be achieved via a connected vacuum pump. The interior of the cell is 455 mm in height and 250 mm in diameter. The top flange houses a number of feedthroughs, such as a connector to the vacuum pump, the connector to the gas in- and outlet, the feedthrough for voltage and signal cables, as well as the cooling system. The cooling system consists of an outside connector to a tank of a coolant (in our case liquid nitrogen), which is then directed through a copper coil in the inside of the cell. This is where it cools down the medium before going back out of the cell and being released into the atmosphere. The temperature inside the cell is controlled by adjusting the flow rate of the coolant. This is done

using a MKS 0248A-50000RV Flow Control Valve connected to a Cryocon Model 32 Cryogenic Temperature Controller. The temperature is read via a PT100 temperature sensor mounted on one of the tiles. Some components of the DAQ system were faulty and had to be replaced. These include an ADC and some cables. Also, not all channels in the amplifier module worked. The cables and connections are partly assumed to be the reason why certain tiles did not give a clean readout, the other reason being a broken tile.

### 3.3.2 Procedure and data acquisition

For the operation of our SiPM tests, several hardware components had to be installed and built. The goal of the setup was to be able to get readings of the SiPMs in two situations:

- All SiPMs being illuminated by a short pulse from a blue LED: The tested model has a reported photon detection efficiency (PDE) of 20% for both the xenon scintillation wavelength (178nm) as well as the blue LED light [41]. From these readings the breakdown voltage can be calculated.

- All SiPMs with no illumination: In this configuration, theoretically no signal is expected to be detected by the SiPM. However, signals due to thermal radiation of the electrons jumping to the conduction band can arise and might be picked up by the SiPMs [42]. This gives rise to the main problem of SiPM operation: *Dark count rate (DCR)*. If the detected amount of these unwanted signals (dark counts) is too high, no statistically significant statement can be made, whether a detected signal in a detector is actually due to a WIMP interaction, or just from a dark count. Traditionally this has been a major downside of SiPMs compared to traditional PMTs, with dark count rates normalised per area of recent models still being higher by a factor of 80 than the PMT alternative [1].

In this work, the DCR for the tested SiPM model was estimated. Studying dark counts also allows for the observation of a further phenomenon of MPPCs: *Crosstalk.* A crosstalk signal can occur when an electron released to the conduction band of one pixel is accelerated, scatters with the material and releases another photon. If this photon then hits a different pixel, it can trigger another avalanche. Crosstalks can be potentially observed, as they are detected at close to the same time than the primary signal, increasing its amplitude. The quantity of crosstalk is commonly expressed by the *crosstalk probability* (CTP) [42], giving the rate of crosstalks per

detected darkcount. In this work the external CTP of the tested SiPM was estimated. Setting up LArS for this illumination of the SiPMs with the LED required a special setup shown in fig. 9.

The top flange had threaded holes from previous experiments, through four of which threaded metal rods were fitted, extending just beneath the copper coil. There, a circular PTFE disk was connected to them. This disk served to main purposes: First, it had a small circular hole in the centre, through which the blue LED was put through. The threaded rods held the LED with tape

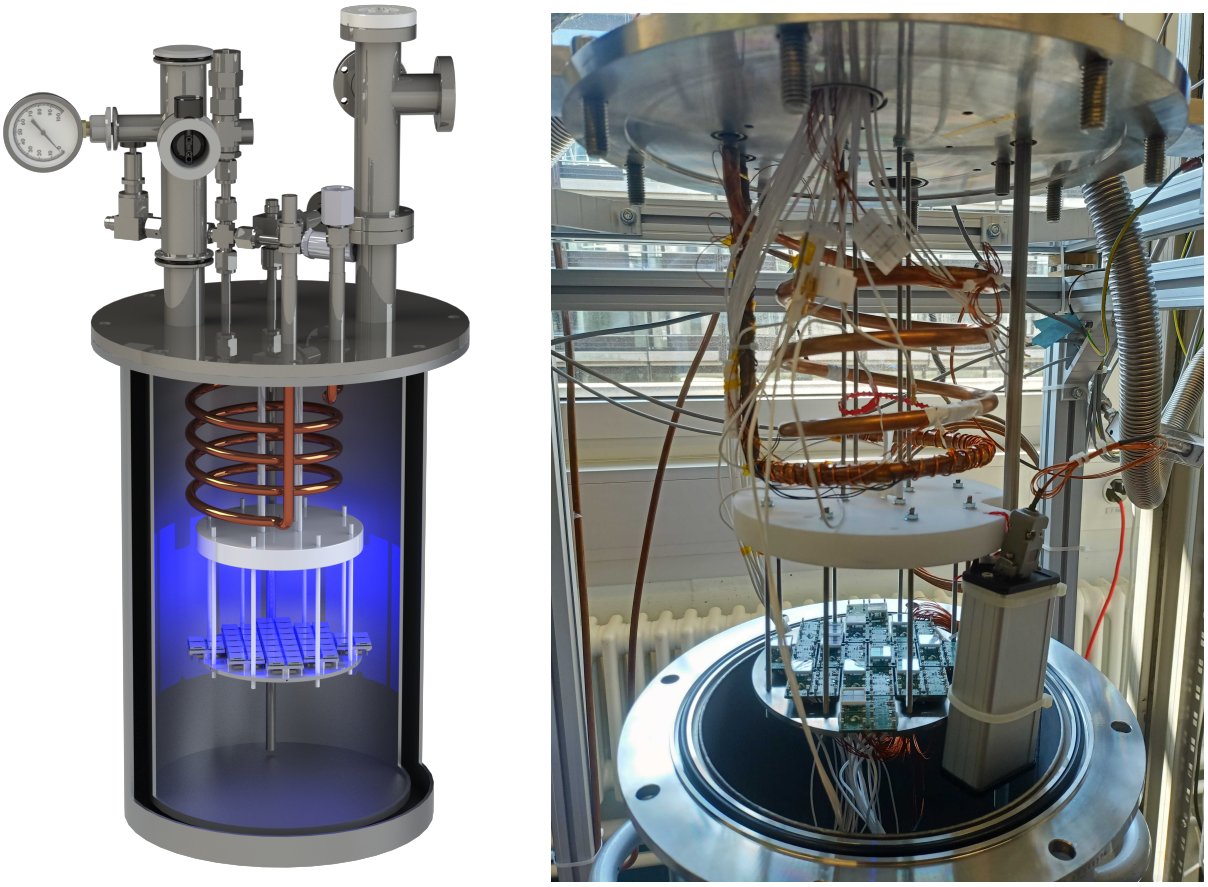

***Figure 9:*** *(left) A render image of the LArS cell with the full top array mounted in the testing setup, illuminated by the blue LED. Below the cooling coil inside the pressure vessel, the top array is held by metal rods to a PTFE disk, which at its center houses a blue LED, illuminating the array. (right) A Photo of the opened LArS cell with the tested SiPMs mounted. The PTFE disk is connected through the inside of the cooling coil to the top flange. As every 4 × 4 only gives one output, there is only one 2 × 2 SiPM mounted to each one. Power and data cables are directed outside through the top flange.*

and cable ties, which was right at the tip of the cable, and barely extended down from the bottom of the disk. Second, it attached the top array to the assembly by eight shorter threaded rods, screwed into the stainless steel baseplate of the top array. The distance from the top array to the LED at the bottom of the PTFE disk was then ∼20-25 cm. This was the maximum possible distance, as on the underside of the top array, all the signal and voltage cables needed space to be bundled and then led back upwards to the feedthroughs via a small cutout in the PTFE disk. A larger distance between the array and the LED could have made the signal strength more homogeneous for the different SiPMs, as now the light intensity for the SiPMs directly below the LED was much stronger than those on the sides.

### 3.3.3 Data acquisition

Before any data is taken, the *baseline* of the signal was calculated. The baseline is the average noise level of the readout when the LED is off. This is done by running a dedicated program which iterates over the bounds of this value until it is fixed for each channel readout. This level is then set as a configuration in the DAQ. The used ADC is 14-bit (so a range of 16384), and as detected signals are negative, the baseline is set to 15500.

For LED ON operation, the LED was set to square pulses of 30 ns, operated at the highest possible amplitude, such that none of the SiPMs would saturate. In this case, the amplitude was 3.25 Vpp for a pulse. A new pulse cycle started every 10 $\mu$s. The TTL sync was connected directly to the ADC. The ADC could hence be set to start data-taking for a new waveform in a precise time interval in respect to the pulse. The ADC recorded 50000 waveforms of 7000 ns in length, set to trigger 3000 ns before the light was pulsed. The main peak of light in the waveform was thus expected at 3000 ns. Data has been taken for operating voltages between 46.0 V and 51.5 V in 0.25 V increments, at temperatures ranging from 170 K to 200 K in 5 K increments.

For LED OFF operation, the ADC recorded 100000 waveforms of 0.1 ms without trigger, so dark counts can appear throughout the waveform. Data has been taken for operating voltages between 50 V and 54 V, at the same temperatures as for LED ON operation.

The whole DAQ setup can be seen in fig. 10. The datasets were saved on the computer as .ROOT files. The DAQ software has been written in house.

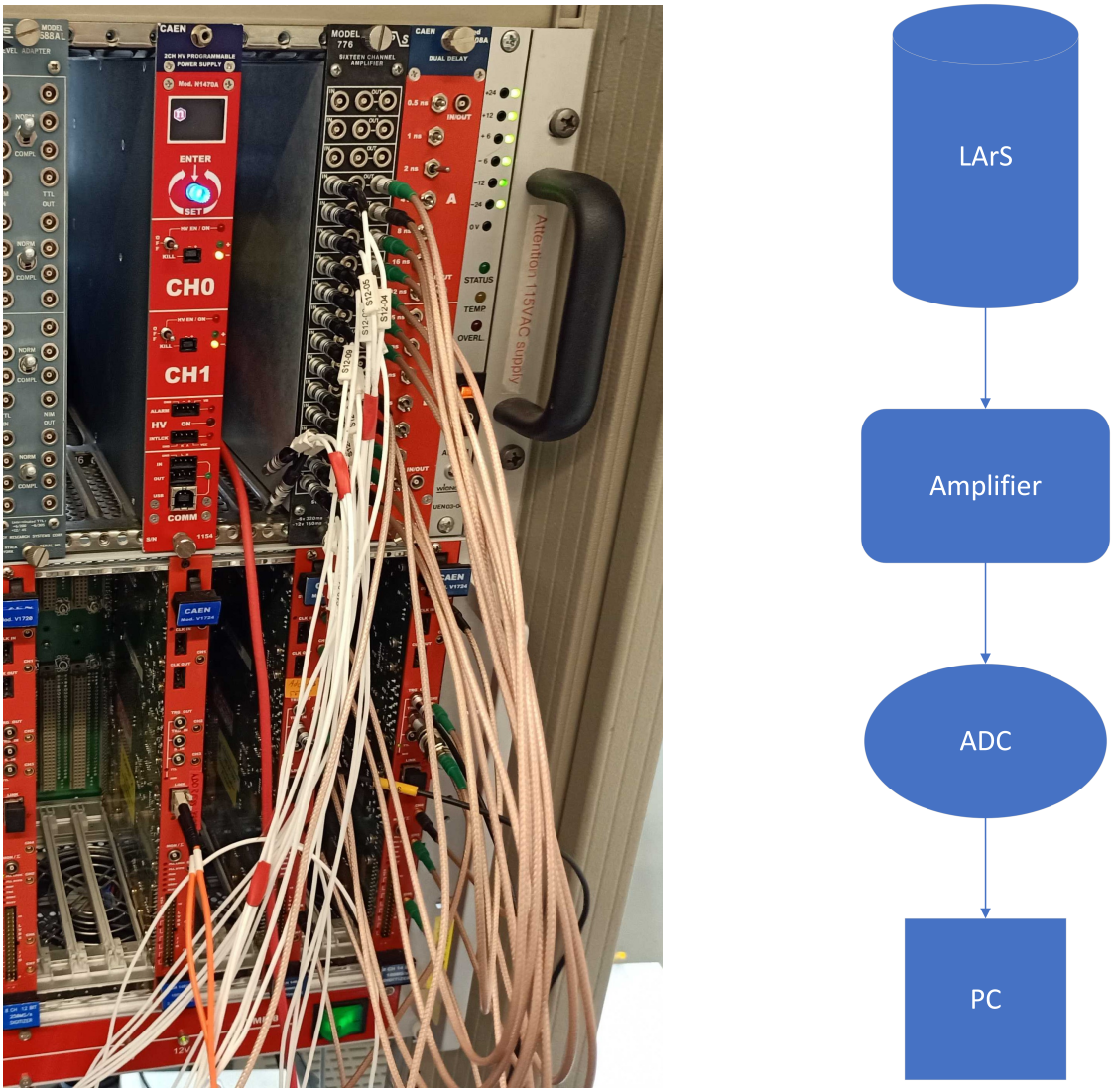


***Figure 10:*** *(left) Photo of the DAQ modules of LArS: The white signal cables connect to the outside amplifier module, which in turn sends the amplified signal via the brown cables to the ADC in the bottom rack. (right) Schematic of the DAQ setup. For each module, a data cable connect via the feedthrough to the amplifier, which then connects the* $\times$ *20 amplified signal to the ADC, where then the digital signal goes to the PC.*

## 3.4 Characterisation techniques and results

In our data taking runs for LED ON and LED OFF operation, data was acquired for 12 SiPMs out of the total 48 that will make up the top array. Out of these 12 loaded SiPMs, only 9 have

produced analysable data. For the other three data channels there was a malfunction of one component during the data taking process. Possible culprits could be the SiPM itself, the pre-amplifier, the cables/connectors, the outside amplifier or the ADC. By trial and error with other combinations of the cabling, the malfunction was determined to come from inside the cell, most likely a pre-amplifier or a cable connector. Some of the components, including a SiPM window, were damaged in a previous attempt to close the cell when the array pressed on the copper cooling coil. The SiPM has been replaced, but non-visible damage to the pre-amplifier could not be ruled out at the time. The improved setup seen in fig. 9 prevented further similar accidents.

### 3.4.1 File processing

The data analysis was performed in Python [43], version 3.8.14. To read the ROOT file, the package "uproot" [44] was used. In the read file, there are 50000 recorded waveforms for LED ON operation, and 100000 waveforms for LED OFF operation. The processing of the raw data files is the same for both LED ON and LED OFF runs. One LED ON waveform has 700 datapoints corresponding to the amplitude of the signal for 10 nanoseconds of the waveforms duration. The same is true for LED OFF waveforms, but their duration is 100'000 ns. The processing determines what a peak is in the waveform, and what can be attributed to noise fluctuation. The baseline is recalculated by using the median of the first 50 entries of the waveform (as the trigger position is located at the 300th sample). If a dark count is located in these first 50 entries, the baseline will be slightly skewed, but over the whole 50 entries the process is able to cancel out such effects. We also calculate the root mean square (RMS) from these waveforms. An event is considered a signal once it exceeds five RMS, as seen in fig. 11.

The processing then produces a dataframe with all the identified peaks for a given SiPM readout. For each peak it lists

1. its waveform number (from 1 to 50000, resp. 1 to 100000)
2. its peak number in the waveform, in case there is more than one peak
3. the length or width of the signal (given in number of consecutive samples above five standard deviations above baseline)
4. the position of the peak (number of the first waveform above five standard deviations above baseline), the time of the peak after the start of the waveform

5. the area of the signal, given in units of integrated ADC counts.

Using these values, the aim is to determine the four main characteristics: BV (using LED ON data) and DCR, gain and CTP (using LED OFF data). Also in specific cases, the gain can be computed for low voltage and low temperature LED ON data.

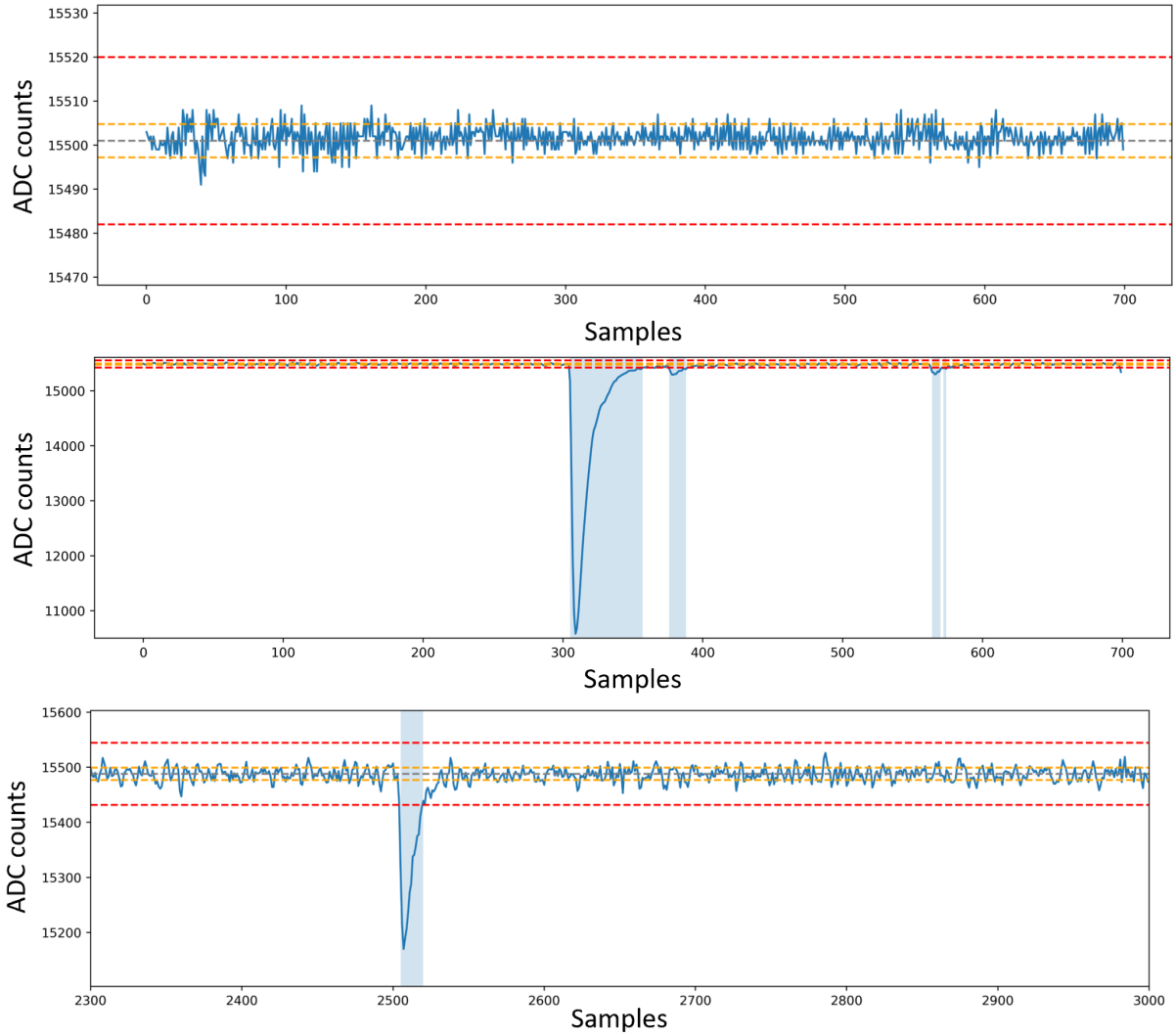


***Figure 11:*** *(top) Example of a LED OFF waveform with no detected signal. (middle) Example of a LED ON waveform with detected signals. (bottom) Example of a LED OFF waveform zoomed into a region with a detected SPE peak. The yellow dotted lines denote one standard deviation from the baseline, the red dotted lines 5 standard deviations, marking the threshold where a signal is detected. The blue shaded region is considered a peak.*

### 3.4.2 LED ON: Breakdown voltage

As mentioned before, the breakdown voltage is the voltage at which point the APD first functions in Geiger-mode, thus where consistent signals can be recorded. To find this voltage, the areas of the observed peaks are studied. Of importance to the calculation of the BV are only the primary peaks by the LED, such as the first, large peaks in fig. 11 (middle) and not the ones at higher sample numbers, which are called *afterpulses* caused by electrons trapped in impurities of the silicon layer, which are later ejected, producing new avalanches [42]. The peaks to be included in the statistics and plots are selected by filtering. For LED ON operation, these are done by observing the histograms for length and position. In fig. 12 left, the peaks of higher length signals are clearly visible and distinguishable from the short length noise and afterpulse signals, which in this figure go up to length values of 12 samples. Making a cut to only select signals with a length of over 12 samples long would thus be applied to such a distribution. As some SiPMs are more or less illuminated, these length values are not uniform, and length cuts have to be adapted accordingly for different SiPMs. Also in the position histogram in fig. 12, the afterpulse population is clearly visible with a distribution at a peak around 450 ADC counts. Nonetheless, it does not imply that afterpulses are most frequent at this position: As position data only records the start of the

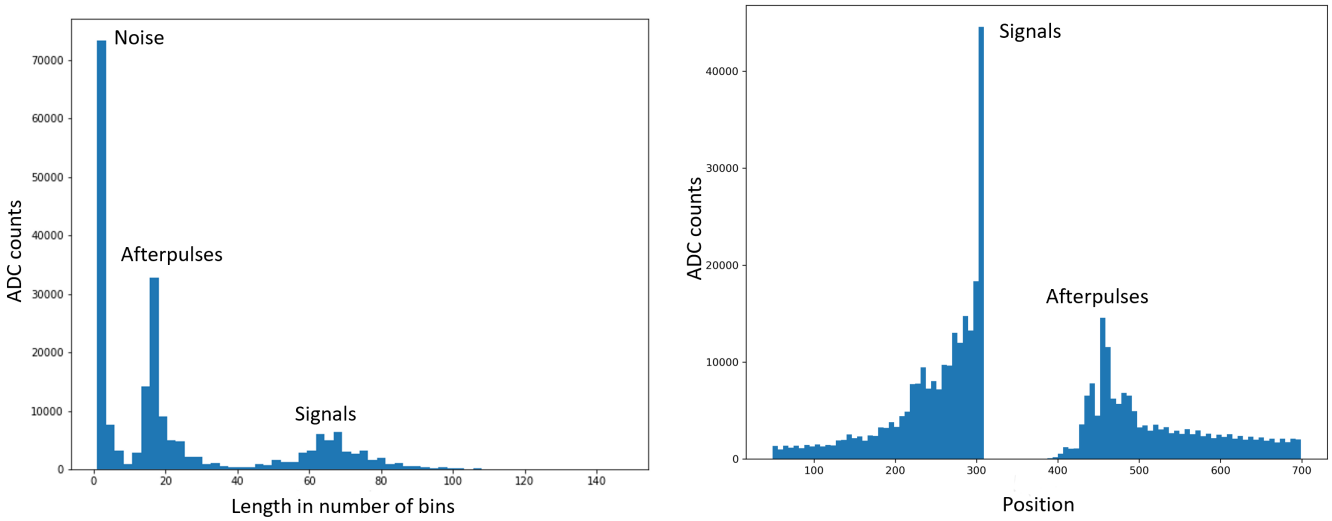


***Figure 12:*** *(left) Example of a typical LED ON length histogram each bin number corresponds to length value. (right) Example of a typical LED ON position histogram. The primary signal peak is clearly visible at 300 samples, with afterpulses around 400-450 samples.*

signal, no new positions are recorded as long as the preceding signal is still above the 5 standard deviations threshold. In reality, the afterpulses before 450 samples are included in the length and area of the main LED signal, leading to slightly larger values for these main peaks.
Meanwhile, the primary LED signal sits around 300 samples, as expected by the coordinated trigger. Signals before the primary LED signal are expected to be noise and dark counts. The exponential increase in signals leading up to the 300 samples is still not well understood. Possible explanations might be that this effect is due to different times that the LED takes turning on.
As the peak position is indifferent from illumination of the SiPMs, a general cut to only select signals with positions between 290 samples and 320 samples has been made for every SiPM at every voltage and every temperature.
With length and position cuts, the dataset is now mainly comprised by the primary LED signals. As a first step, a histogram of a single channel at a temperature for different voltages is observed. As seen in fig. 13, the distribution of the areas appear to be Gaussian in shape, and can also be fitted with Gaussian curves [1].

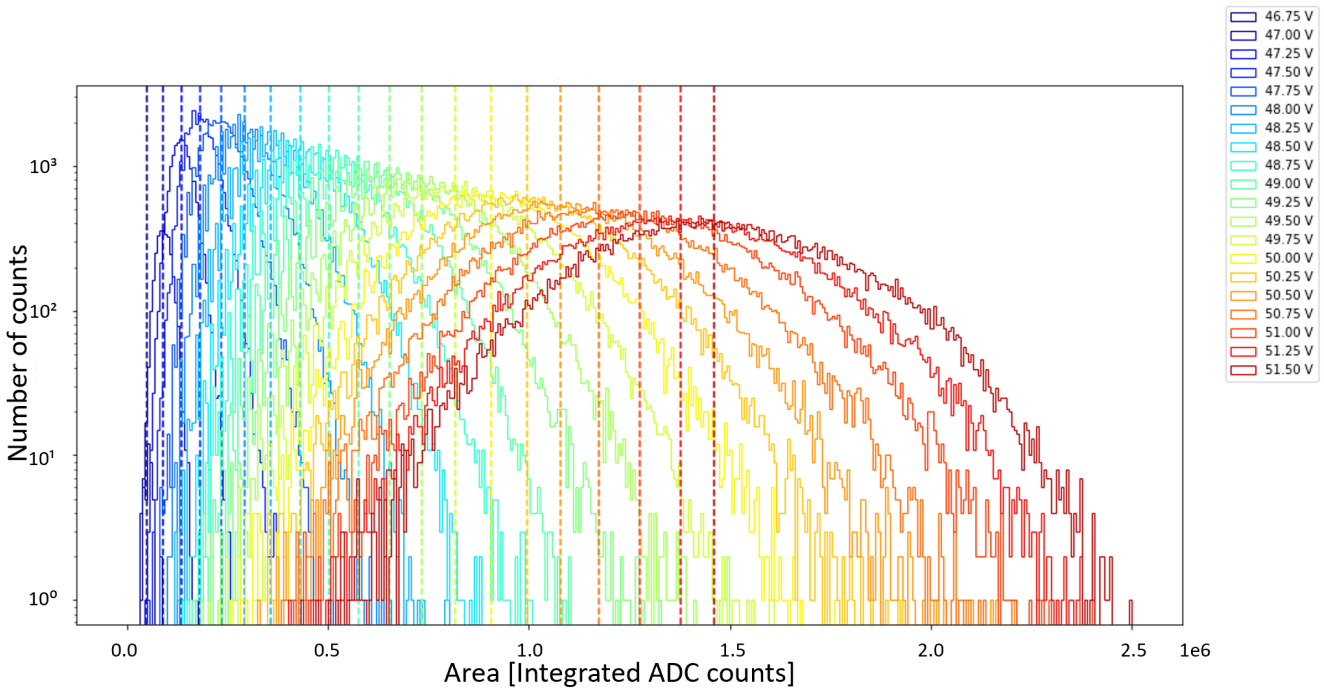


***Figure 13:*** *Histogram of area curves, with a vertical line at the median value of the area distribution for each voltage*

The breakdown voltage is defined as the voltage at which the peak of this area curve reaches 0. The peak can be calculated using a Gaussian fit of the curve, but can be approximated by calculating the median of the dataset. In fig. 13, the median of the area curve for each voltage is depicted by a vertical line at that value. Plotting these median areas against their bias voltage, we observe a trend which can be fitted using a $y = a\sqrt{x} + bx + c$ function, seen in the red dotted line in fig.14

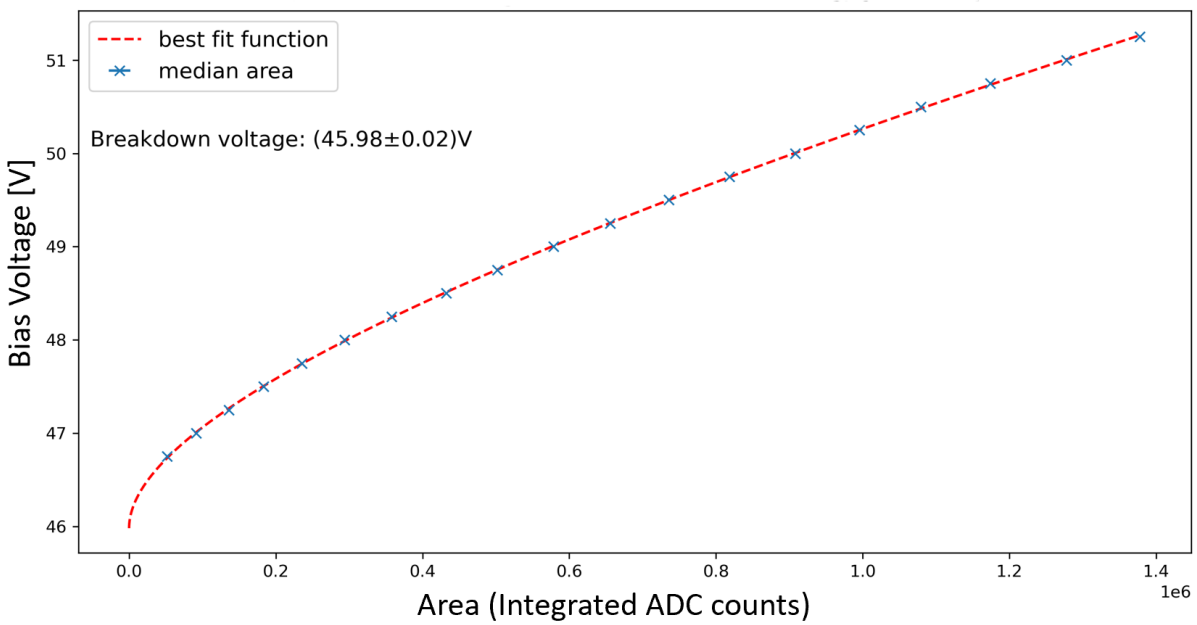


***Figure 14:*** *Example of the fitted regression for median area values of different voltages.*

The breakdown voltage is found by evaluating the fitted function at x = 0 (which corresponds to area = 0). This process is now done for each SiPM at different temperatures. A plot of the different calculated breakdown voltages and their temperature dependence can be seen in fig. 15. As the figure shows, the values for breakdown voltages and their respective uncertainties – due to the fit function not always being able to fit the data – show considerable discrepancies of up to 1 V. Although precise statements about the BV uniformity through the sample of MPPCs cannot be made, a clear linear increase with increasing temperature can be observed. Even the highest BVs does not exceed 47.5 V at 195 K, thus voltages above 50 V would pose optimal operating conditions, as it was observed with previous SiPM models [1]. A future study of BV data for all 48 SiPMs for the top array will provide more information about this trend.

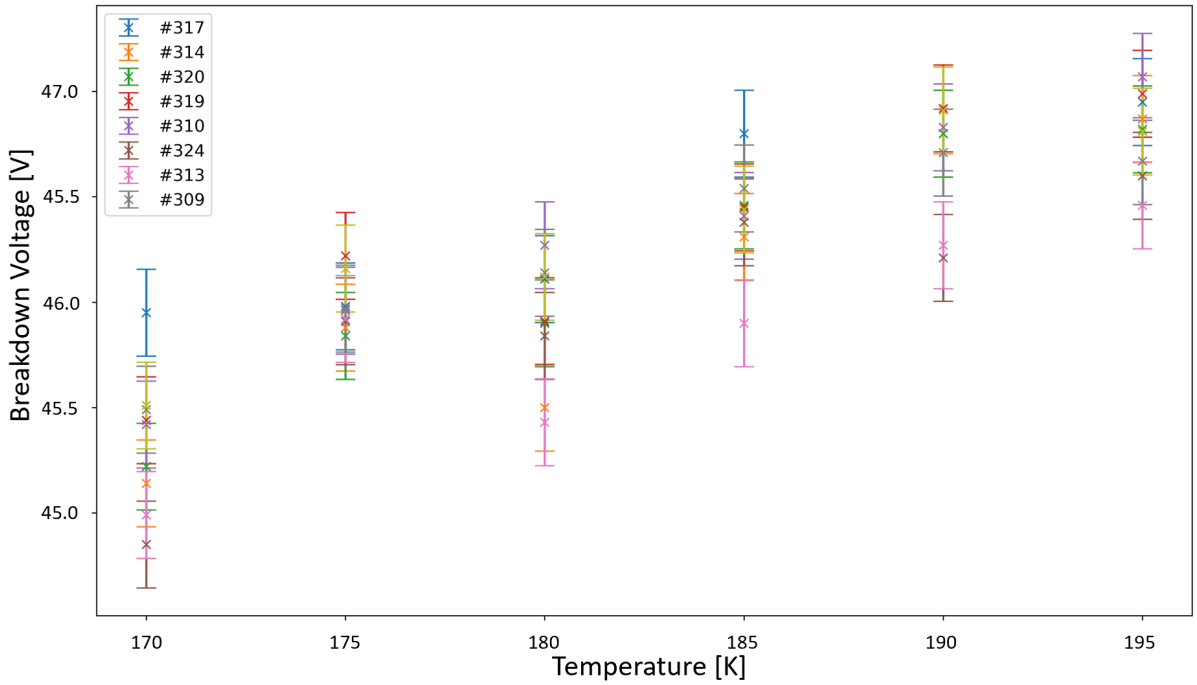


***Figure 15:*** *Breakdown voltages at different temperatures for eight datasets. The number in the legend is the number given to a specific SiPM. The plot shows a linear increase in breakdown voltage with increasing temperature*

### 3.4.3 LED ON: Gain extrapolation

The strength of a signal is determined by the number of photons that hit the SiPM, namely how many APD are triggered in the MPPC matrix, and the operation voltage. Observing the area of the signals at lower voltages, distinct peaks can be identified for different numbers of photoelectrons released, as seen in fig. 16.
The gain is calculated as

$$G = \frac{Q}{q_\mathrm{e}}, \tag{3}$$

with $q_\mathrm{e}$ the elementary charge and

$$Q = \int I\mathrm{d}t = \frac{1}{R \cdot F_\mathrm{amp}} \int V\mathrm{d}t = \frac{ADC_\mathrm{range}}{R \cdot F_\mathrm{amp} \cdot ADC_\mathrm{res}} \int ADC_\mathrm{counts}\mathrm{d}t, \tag{4}$$

where Q is the total charge released throughout all avalanches in the SiPM, R is the impedance of the ADC (50 Ω), $\mathrm{F_{amp}}$ is the total amplification factor (x 10 for the pre-amp and×20 for the

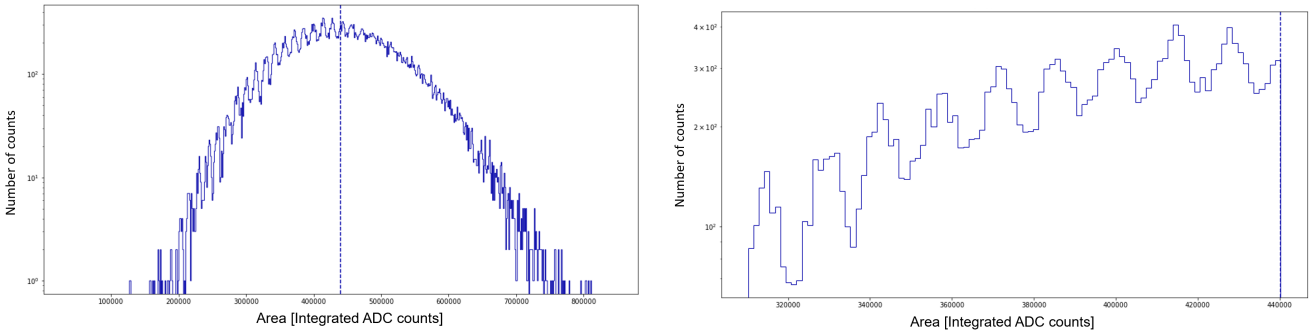


***Figure 16:*** *(left) Example of an area histogram with distinct PE peaks to the left of the median line. (right) Zoom into the histogram to visualise the different peaks.*

amplifier module for a total of 200 ×), $\mathrm{ADC}_{\mathrm{res}}$ is the resolution of the ADC (14 bit, hence 16384), $\mathrm{ADC}_{\mathrm{range}}$ is the total voltage range of the ADC (2.25V) and $\mathrm{ADC}_{\mathrm{counts}}$ is the difference between the mean area value for an $n$ PE peak and an $n+1$ PE peak. This corresponds to the mean area for a single photoelectron (SPE) peak, as the gain is defined as the number of released electrons by the avalanche caused by one photon hitting the MPPC. As the number of photoelectrons which comprise the peaks in fig. 16 is unknown, the distance between two peaks is calculated, by smoothing the histogram and taking the peaks of the resulting curve, as seen in fig. 17.
This method allows us to consider multiple peaks and the distances between them. To get a singular value, the mean distance between these selected peaks is taken, as seen in fig. 18.
Using this $ADC_{\mathrm{counts}}$ value of $14116 \pm 481$ in in eq. 4, we arrive at a charge $Q = (1.922 \pm 0.004) \cdot 10^{13}$ C and a gain of $G = (1.20 \pm 0.05) \cdot 10^6$ for this SiPM at 47.5 V and 170 K. Repeating this process at 48.5 V and again 170 K, we arrive at a gain of $(1.92 \pm 0.05) \cdot 10^6$. Assuming gain increases linearly with voltage (which LED OFF data will strongly suggest), we can extrapolate this trend to higher voltages. Unfortunately, at voltages exceeding 49 V, this method fails, as the distinct PE are no longer recognisable, as the area histogram smooths out, as seen in fig. 13. However, using the extrapolation, an estimate can be made assuming the suggested increase of gain by $(0.72 \pm 0.05) \cdot 10^6/V$. Therefore, at 170 K and 52 V, a gain of around $4.5 \cdot 10^6$ would be expected. As will be seen below, this is a slight overestimation.

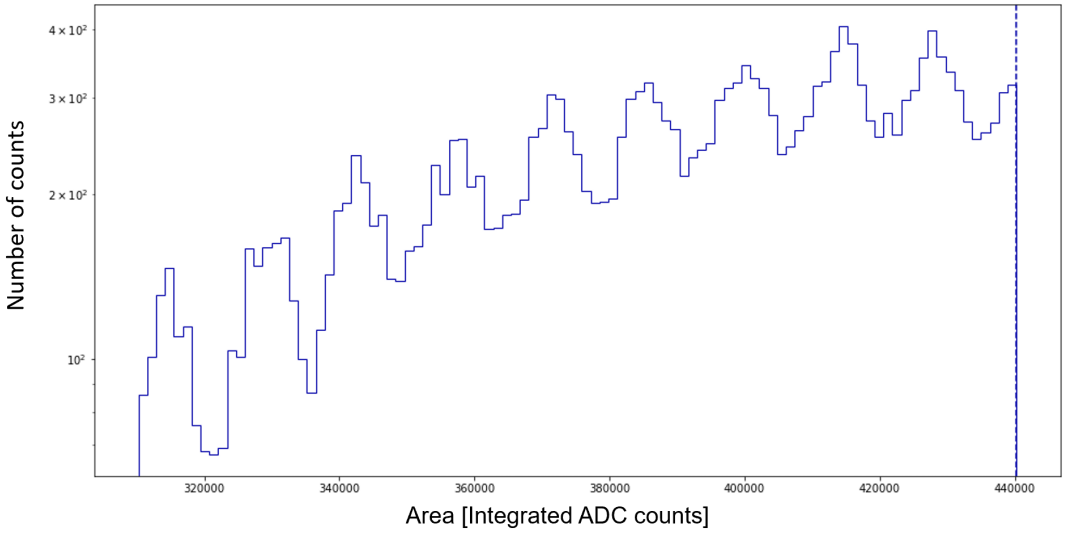


***Figure 17:*** *Multiple PE peaks in black and the data with smoothing filter in blue. The dotted lines denote the local maximas and minimas of the smoothed histogram.*

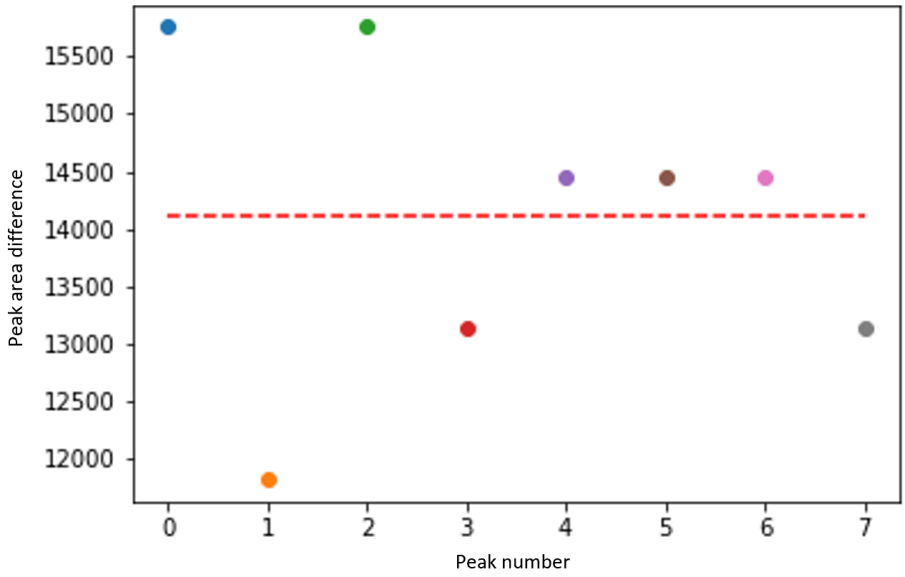


***Figure 18:*** *The dots in this graph show the distance between neighbouring PE peaks in ADC counts, with a fit line denoting the average distance between the peaks, here* $14116 \pm 481$.

### 3.4.4 LED OFF: Dark count rate

With the LED turned off, all the light signals the SiPMs detect will be dark counts and noise, the difference being that dark counts are spontaneous detections of light signals where none are expected, often caused by thermal or quantum mechanical effect. Noise on the other hand denotes false signals caused by electric components or external interference, for example. Using similar cuts as with the BV tests, we arrive at a set of signals indistinguishable from those by the LED. Fig. 19 shows the area histogram for one SiPM without any cuts made. Noise can be clearly seen as the peak around area equal 0. The red vertical lines highlight the median area of the 1 PE and 2 PE peak. The 3 PE peak is no longer clearly recognisable. Behind each peak follows a "shoulder" of signals, the origin of which is not clearly understood, but was also reported in literature characterising the same MPPC model [45]. To select what is considered a dark count and not noise, the rule is to count all the signals with an area larger than half the median area of the 1 PE peak, so the "0.5" PE area. What is then selected as dark counts is what could hardly be distinguished from actually wanted signals.
To determine the precise position of the 1 PE peak, an adequate signal width cut is determined. Because triggers happen at random times, the position of the signal is no longer bound to the time trigger as before. Fig. 20 shows the region around the SPE peak with various cuts. Ideally, the cut is chosen such that all the signals before the clearly visible Gaussian peak are removed, without removing signals within the peak. In this case, lengths of 12 bins and over result in a clean selection. The area histogram can now be integrated over all the number of datapoints starting at

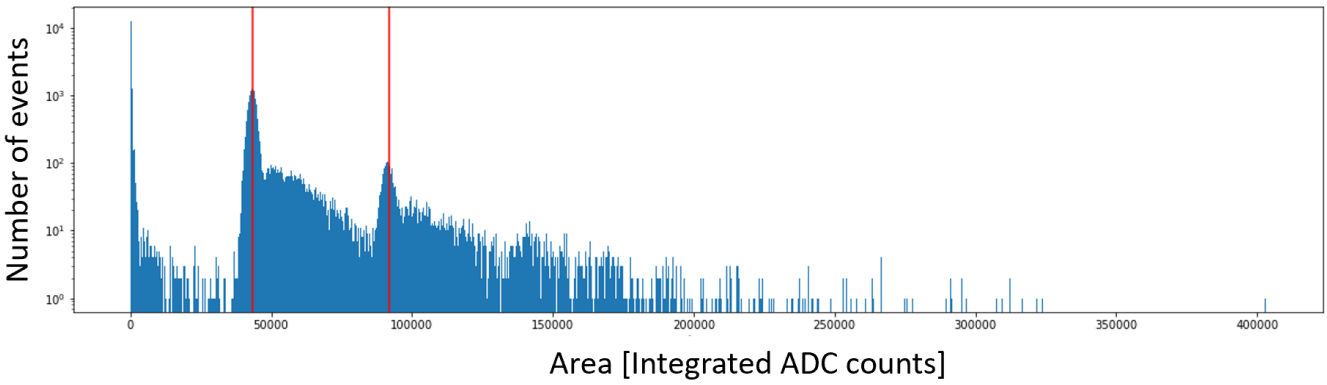


***Figure 19:*** *LED OFF Area histogram with no cuts. The red vertical lines indicate the 1 PE and 2 PE peaks. Noise is seen as the peak around an Area of 0.*

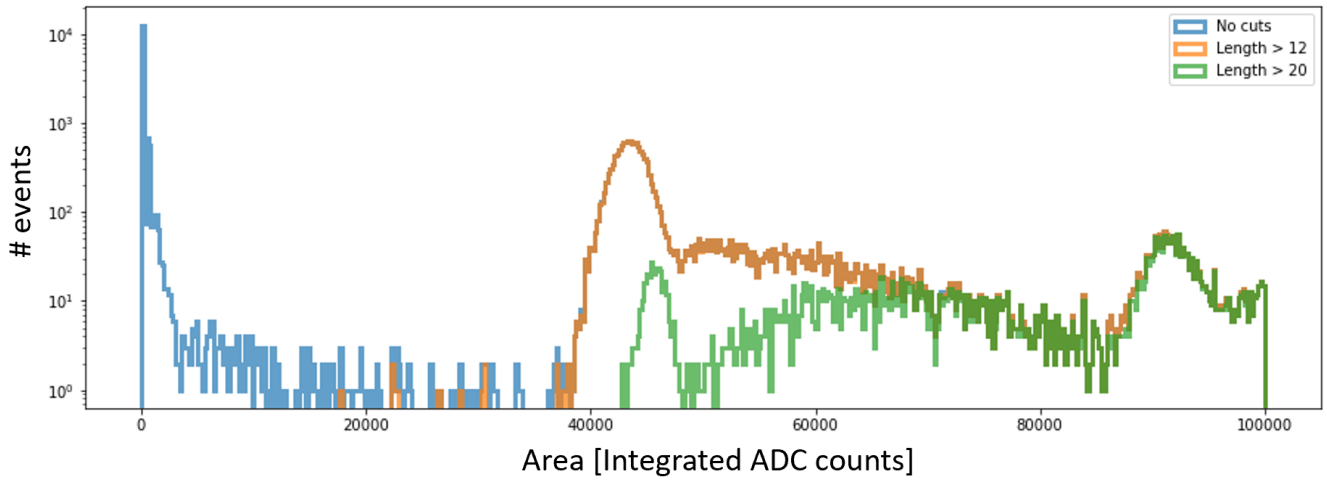


***Figure 20:*** *Histogram of LED OFF peak area with different cuts. No cut includes too much noise, whilst only selecting lengths of > 20 also cuts away a large portion of the SPE peak.*

different area values, and then the derivative of the resulting curve can be determined. As most of the events are in the 1 PE peak (notice that the y-axis in fig. 20 is in log scale), we expect a sharp peak in the derivative at that point. As seen in fig. 21, this peak is indeed very prominent and allows for a clear definition of the SPE peak.

Knowing the centre of the peak from the minimum of the derivative (dotted line in fig. 21), a Gaussian fit can now be applied to the peak with the parameters of the fit allowing for the calculation of the DCR. Thus the median $\mu$ gives the position of the peak from which the 0.5 PE position can be determined. The DCR is now the number of detected signals above 0.5 PE, divided by the area of the SiPM and the acquisition time. The DCR can be computed for the acquired datasets for temperatures ranging from 170 K to 200 K and voltages ranging from 50 V to 54 V. These are typical operation voltages, with temperatures in the TPC gas phase expected to be around 190 K. The DCR can be directly plotted against the voltage at which the data was taken. This voltage can be expressed as the voltage above BV, or *over voltage*. As seen in fig. 22, there is a linear increase in DCR with increasing over voltage, with DCR decreasing for lower temperatures.

As the top array will only be operated at a single voltage, it makes sense to compare the data for different channels at a specific bias voltage, in this case 52 V. As visible in fig. 23, the variation in DCR values for different SiPMs can change substantially, especially for higher temperatures (note that the y-axis is in log scale). The DCR remains very high compared to PMT candidates [1].

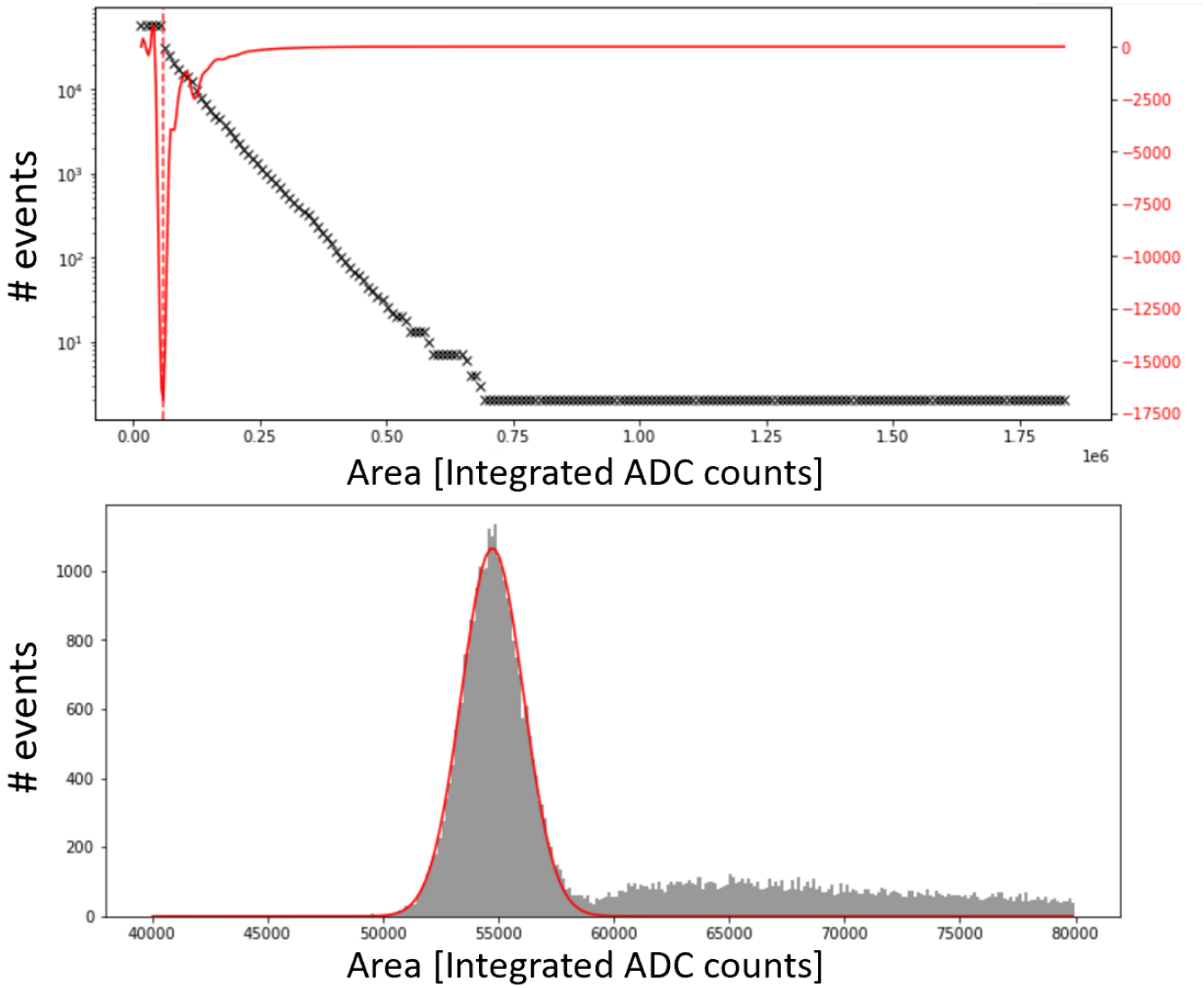


***Figure 21:*** *(top) Integral of the total area of the signals for different starting points (black crosses), and the smoothed integral of this resulting curve (red). (bottom) SPE peak fitted with a gaussian function.*

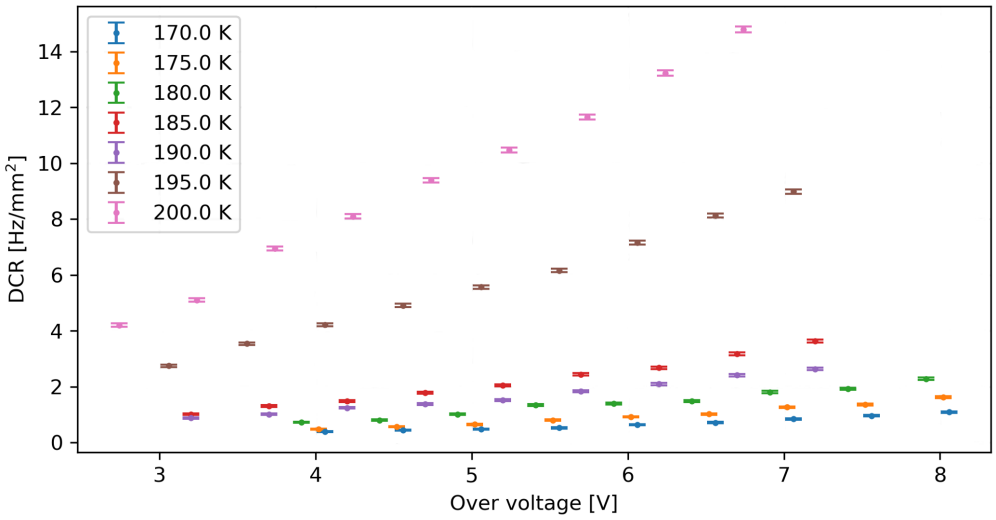


***Figure 22:*** *DCR for different temperatures versus over voltage. The DCR increases for higher temperatures and higher voltages. The slope for the increase is higher for larger temperatures, as they result in more thermal radiation.*

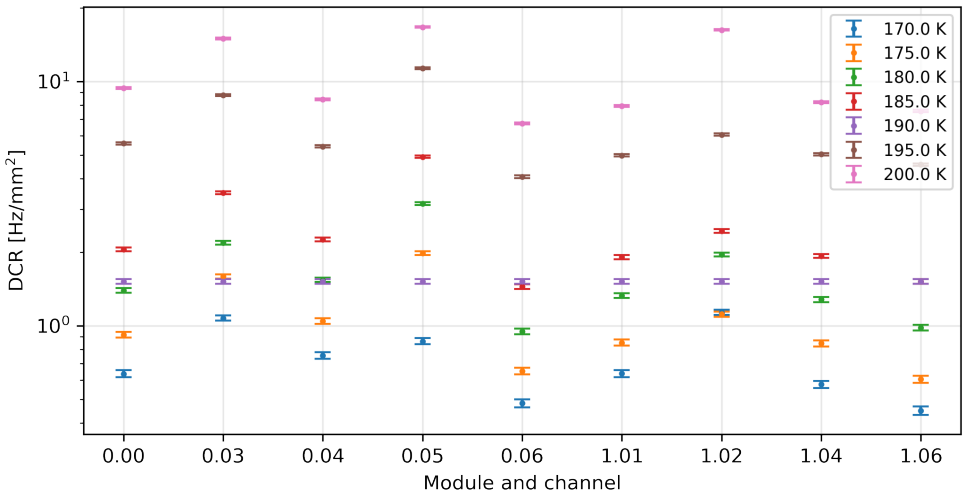


***Figure 23:*** *DCR for different channels at different temperatures at 52V. The plot shows some variance between different channels, but a general increase of DCR with increasing temperature. In the x.yy format, x stands for module number, and yy for the channel number in this module.*

### 3.4.5 LED OFF: Gain

As mentioned in section 3.4.3, the gain for higher voltages and temperatures cannot be calculated with LED ON operation, but only estimated by extrapolation. Using LED OFF data, the gain can be directly calculated for all temperatures and voltages. The $ADC_{counts}$ value in eq. 4 simply becomes the $\mu$ value of the Gaussian fit of the SPE peak, as discussed in section 3.4.4. Plotting the gain against the bias voltage (see fig. 24), we see a clear linear increase of gain with increasing bias voltage, and a decrease in gain for increasing temperature. The data for T=190 K appears inconsistent with the data for other temperatures. From the evolution over time, we infer that the measurement was started when the temperature in the cell was still 185K, and during the course of the measurement gradually increased to 190 K.

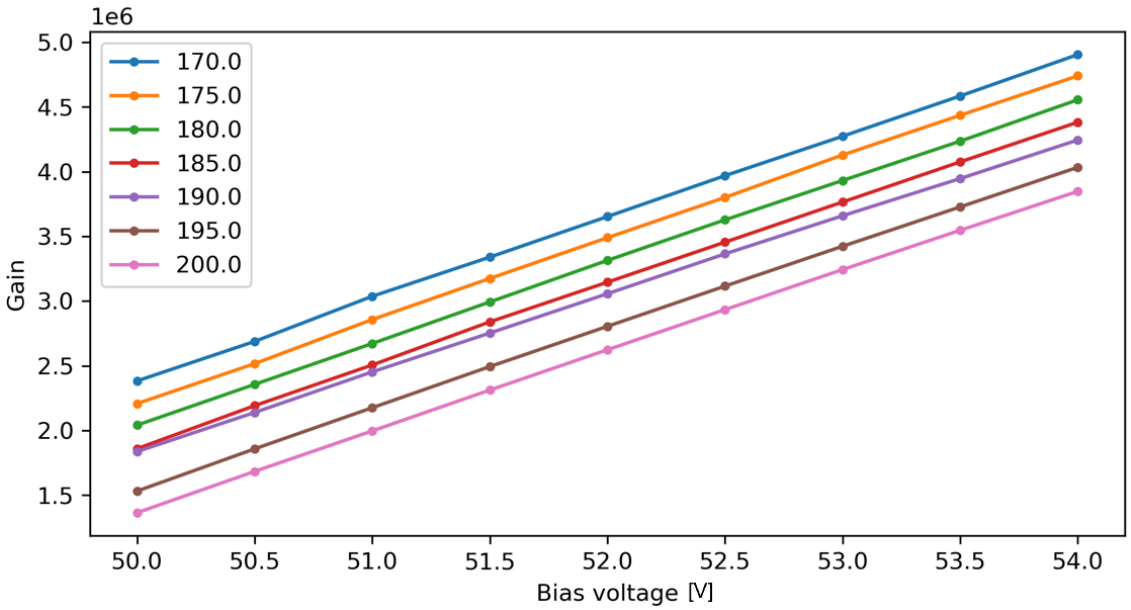


***Figure 24:*** *Gain versus bias voltage. The gain clearly increases linearly with bias voltage and at the same rate for different temperatures. The data points are connected with lines to demonstrate the spacing due to different temperatures.*

However, if we can plot the gain against the over voltage (see fig. 25), we see that there is very little temperature dependence for the same over voltage. Having gain and DCR increasing with increasing voltage poses a problem, since high DCR should be avoided, whereas high gain is ideal. We can compare the relation of gain and DCR by plotting them against each other. From the linear dependence of DCR and over voltage, and the linear dependence of overvoltage and gain, a

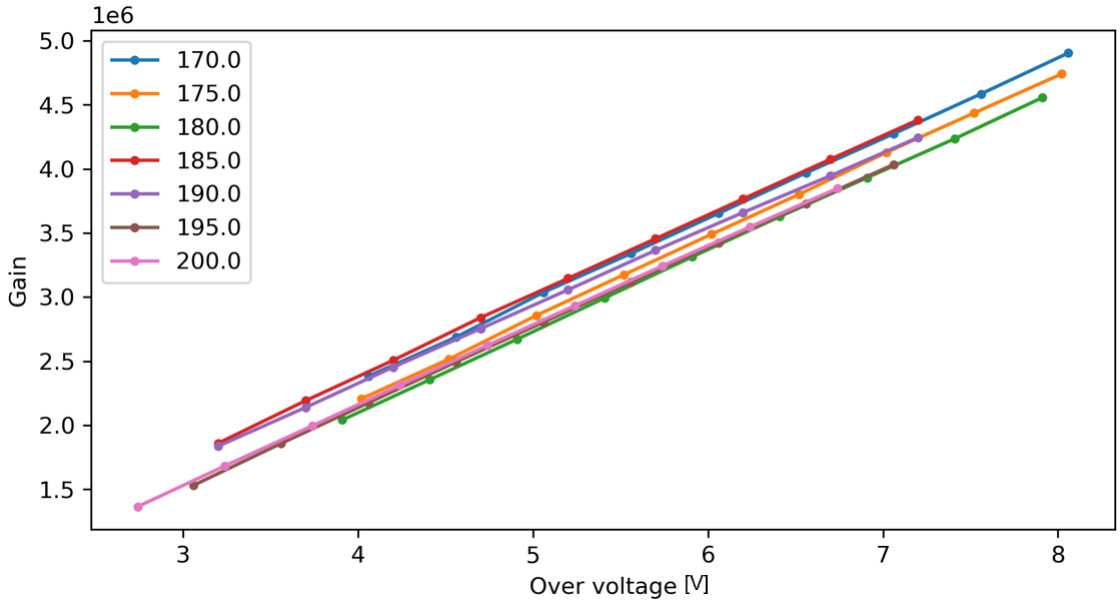


***Figure 25:*** *Gain versus over voltage. Whilst gain still increases linearly with increasing voltage, there appears to be no more temperature dependence, as there is no spacing between the data points connected with lines.*

linear dependence between DCR and gain is expected. Fig. 26 shows that the data in fact follows this trend.

As with DCR, it makes sense to observe the gain differences for the different channels. Again at 52 V, fig. 27 shows that gain remains similar across the different channels.

### 3.4.6 LED OFF: Crosstalk probability

Even for the highest recorded DCRs here, the probability that two dark counts hit the same cell at the same time is very small. The fact that 2 PE or even larger signals are detected, can thus mostly be explained by crosstalks. The crosstalk probability is calculated as

$$CTP = \frac{DCR_{1.5PE}}{DCR_{0.5PE}}, \tag{5}$$

where $DCR_{1.5pe}$ is the DCR, but only for signals above 1.5 PE, set as the threshold for signals closer to the 2 PE peak than the SPE peak. $DCR_{0.5PE}$ is the DCR as calculated above. Plotted against the gain in fig. 28, a linear increase of the CTP with increasing gain is visible. This is

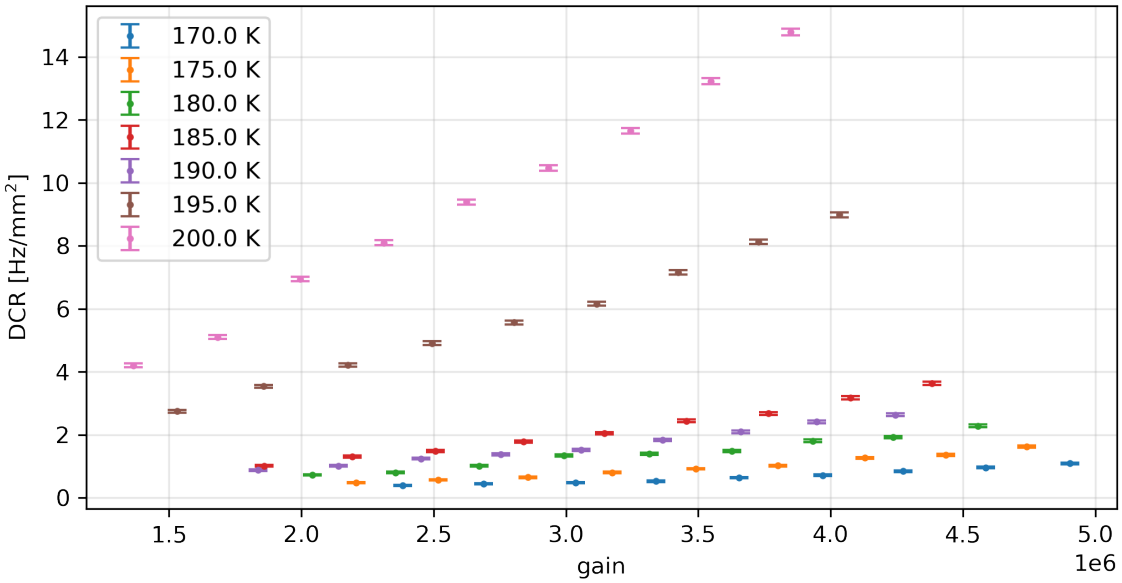


***Figure 26:*** *Dark count rate versus gain. The DCR increases with increasing gain. The slope of the increase becomes steeper with increasing temperature due to there being more thermal radiation.*

because crosstalks are caused by the electrons released into the conduction band and releasing a photon when scattering with the material. As the released electrons account for the gain, a linear dependence between gain and CPT was to be expected. For low gains, the CTP appears to approach zero, although a base CTP for very low gain cannot be ruled out.

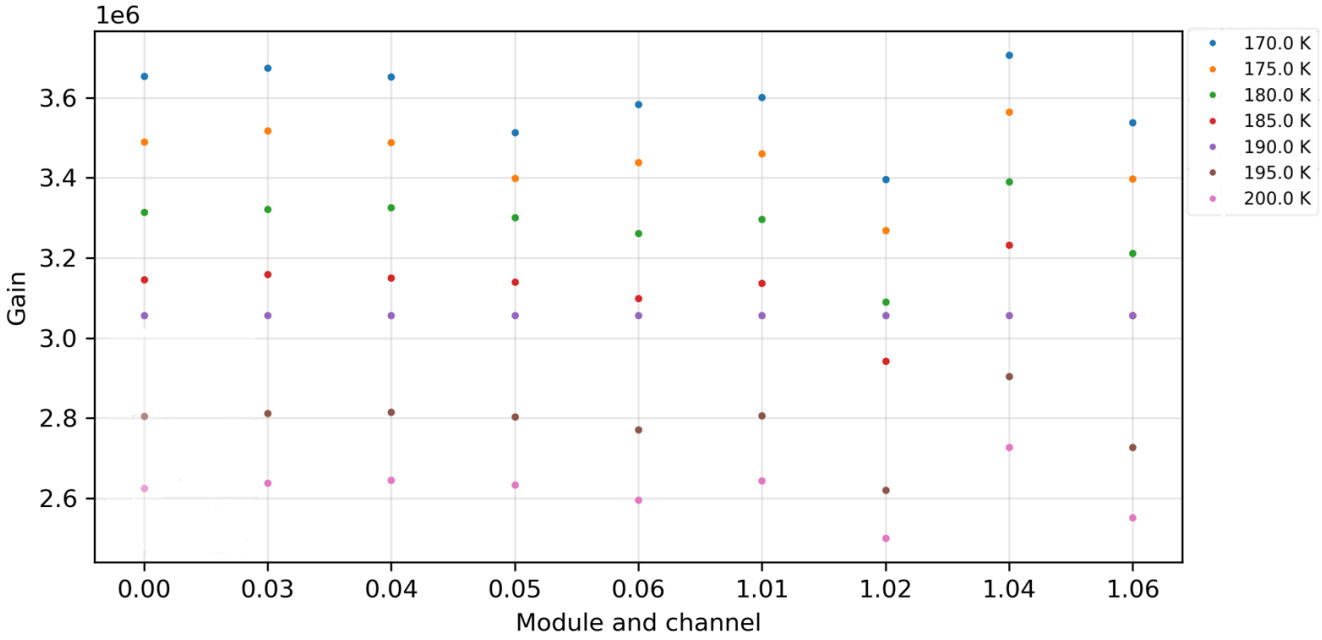


***Figure 27:*** *Gain for different channels at 52V. In the x.yy format, x stands for module number, and yy for the channel number in this module.*

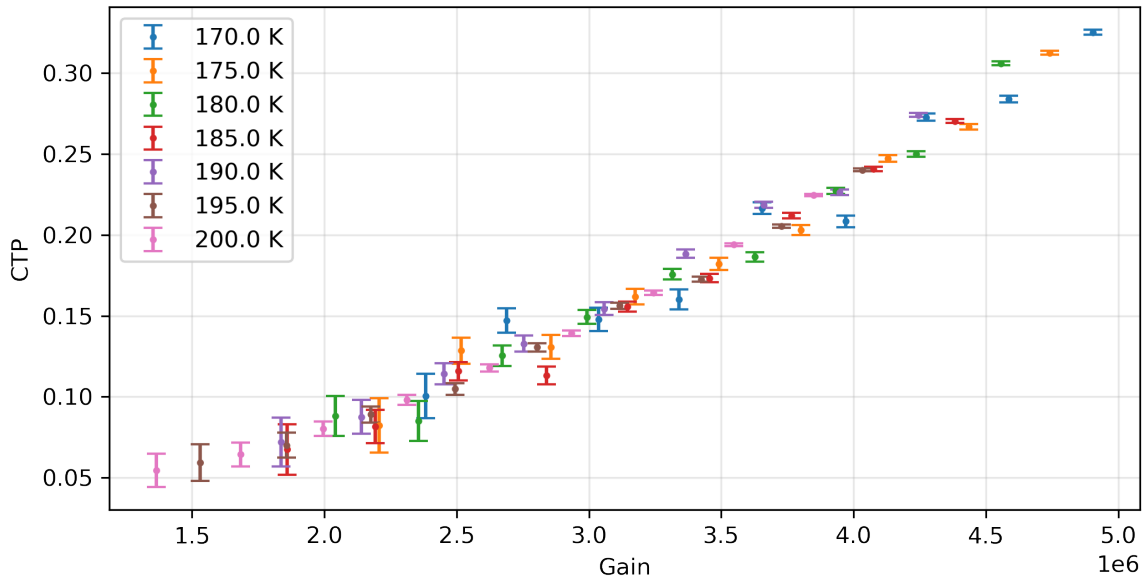


***Figure 28:*** *Crosstalk probability plotted versus gain at different temperatures and different gains. The CTP increases linearly with gain. For low gain, the CTP appears to approach zero. Data is for module 0 channel 0.*

# 4 Conclusion and Outlook

A set of VUV4 S13371-6050CQ-02 MPPCs produced by Hamamatsu Photonics where characterised using the Liquid Argon Setup at the University of Zürich. The results obtained from this characterisation are in agreement with results of characterisation of previous models and show improved performance in certain areas, such as gain [1]. The breakdown voltage of the SiPMs has not decreased by a significant amount, being on average $(46.5 \pm 0.5)$ V at 190 K. However, the gain at $3 \cdot 10^6$ at a bias voltage of 52 V and a temperature of 190 K has increased substantially from previous models [1]. At this gain and temperature, the crosstalks were measured to happen in 15% of all signals. The main argument against the use of SiPMs in DM detectors, namely the high DCR of $\mathcal{O}(1\text{Hz/mm}^2)$ at 190 K is still an important factor in this latest generation of photosensors.

In terms of the setup, several improvements could be made. The illumination of the SiPMs by the LED was uneven, where the SiPMs right below the LED nearly saturated and the SiPMs on the outside had only small signal peaks. The $2 \times 2$ SiPMs were mounted on a ceramic holder, which is problematic for ultra low background experiments, as the ceramic is known to be radioactive. For this experiment, this could be ignored, as the background noise from the electronics was large. In general, LArS proved suitable for the characterisation, but the diameter of the cell was rather small.
The full top array was installed into the Xenoscope assembly for the TPC phase of the project. In parallel, a decision will be made whether SiPMs will be replacing the PMTs in the DARWIN baseline design, or whether further improvements to the VUV MPPCs DCR have to be made, until they are a viable alternative to PMTs.

# Acknowledgements

First of all I would like to thank my fantastic supervisor Ricardo Peres for his relentless support and help during the whole course of this thesis, investing time he did not have and being a great friend. I thank the head of the research group Prof. Dr. Laura Baudis for her help, giving me the opportunity to work with a fantastic group of researchers. Among them I would like to thank Yanina Biondi, Alexander Bismark and Frédéric Girard for their help, as well as Paloma Cimental and Dr. Jose Cuenca Garcia for letting me borrow their office desks. I thank the electronic workshop for their assistance.

I thank my loving parents and hope I made them proud.

Last but not least, I thank my dear friends who supported me along the way. Cheers, Francesca, Lukas, Dennys, Fabian, Chloé, Alessandra, Hanna, Hannah and Stefanie.

# References


[1] L. Baudis et al. "Characterisation of Silicon Photomultipliers for liquid xenon detectors". In: *Journal of Instrumentation* 13.10 (Oct. 2018), P10022–P10022. DOI: 10.1088/1748-0221/13/10/p10022. URL: https://doi.org/10.1088%2F1748-0221%2F13%2F10%2Fp10022.

[2] K. G. Begeman, Ah Broeils and R. H. Sanders. "Extended rotation curves of spiral galaxies: dark haloes and modified dynamics". In: *Monthly Notices of the Royal Astronomical Society* 249 (1991), pp. 523–537.

[3] M. Markevitch et al. "Direct Constraints on the Dark Matter Self-Interaction Cross Section from the Merging Galaxy Cluster 1E 0657-56". In: *The Astrophysical Journal* 606.2 (May 2004), pp. 819–824. DOI: 10.1086/383178. URL: https://doi.org/10.1086%2F383178.

[4] José P. S. Lemos, Carlos A. R. Herdeiro and Vitor Cardoso. *Einstein and Eddington and the eclipse in Principe: Celebration and science 100 years after*. 2019. arXiv: 1912.08354 [physics.hist-ph].

[5] E. Pécontal et al. "Review of Observational Evidence for Dark Matter in the Universe and in upcoming searches for Dark Stars". In: *European Astronomical Society Publications Series* 36 (2009), pp. 113–126. DOI: 10.1051/eas/0936016.

[6] J. G. de Swart, G. Bertone and J. van Dongen. "How dark matter came to matter". In: *Nature Astronomy* 1.3 (Mar. 2017). DOI: 10.1038/s41550-017-0059. URL: https://doi.org/10.1038%2Fs41550-017-0059.

[7] P. A. R. Ade et al. "Planck 2015 results. XIII. Cosmological parameters". In: *Astronomy &amp Astrophysics* 594 (Sept. 2016), A13. DOI: 10.1051/0004-6361/201525830. URL: https://doi.org/10.1051%2F0004-6361%2F201525830.

[8] Mordehai Milgrom. "MOND theory". In: *Canadian Journal of Physics* 93.2 (Feb. 2015), pp. 107–118. DOI: 10.1139/cjp-2014-0211. URL: https://doi.org/10.1139%2Fcjp-2014-0211.

[9] Constantinos Skordis. "The tensor-vector-scalar theory and its cosmology". In: *Classical and Quantum Gravity* 26.14 (June 2009), p. 143001. DOI: 10.1088/0264-9381/26/14/143001. URL: https://doi.org/10.1088%2F0264-9381%2F26%2F14%2F143001.

[10] David P. Bennett et al. "The First data from the MACHO experiment". In: *Annals N. Y. Acad. Sci.* 688 (1993). Ed. by Karl Akerlof and Mark A. Srednicki, p. 612. DOI: 10.1111/j.1749-6632.1993.tb43945.x. arXiv: astro-ph/9304014.

[11] EROS Collaboration. "Limits on Galactic Dark Matter with 5 Years of EROS SMC Data". In: (2002). DOI: 10.48550/ARXIV.ASTRO-PH/0212176. URL: https://arxiv.org/abs/astro-ph/0212176.

[12] R. D. Peccei and Helen R. Quinn. "CP Conservation in the Presence of Pseudoparticles". In: *Phys. Rev. Lett.* 38 (25 June 1977), pp. 1440–1443. DOI: 10.1103/PhysRevLett.38.1440. URL: https://link.aps.org/doi/10.1103/PhysRevLett.38.1440.

[13] K. Zioutas et al. "First Results from the CERN Axion Solar Telescope". In: *Phys. Rev. Lett.* 94 (12 Apr. 2005), p. 121301. DOI: 10.1103/PhysRevLett.94.121301. URL: https://link.aps.org/doi/10.1103/PhysRevLett.94.121301.

[14] N. Du et al. "Search for Invisible Axion Dark Matter with the Axion Dark Matter Experiment". In: *Physical Review Letters* 120.15 (Apr. 2018). DOI: 10.1103/physrevlett.120.151301. URL: https://doi.org/10.1103%2Fphysrevlett.120.151301.

[15] Dmitry Budker et al. "Proposal for a Cosmic Axion Spin Precession Experiment (CASPEr)". In: *Phys. Rev. X* 4 (2 May 2014), p. 021030. DOI: 10.1103/PhysRevX.4.021030. URL: https://link.aps.org/doi/10.1103/PhysRevX.4.021030.

[16] Carlos Muñ oz. "Models of Supersymmetry for Dark Matter". In: *EPJ Web of Conferences* 136 (2017). Ed. by A. Morselli, A. Capone and G. Rodriguez Fernandez, p. 01002. DOI: 10.1051/epjconf/201713601002. URL: https://doi.org/10.1051%2Fepjconf%2F201713601002.

[17] E. Aprile et al. *Search for New Physics in Electronic Recoil Data from XENONnT*. 2022. DOI: 10.48550/ARXIV.2207.11330. URL: https://arxiv.org/abs/2207.11330.

[18] J. Aalbers et al. *First Dark Matter Search Results from the LUX-ZEPLIN (LZ) Experiment*. 2022. DOI: 10.48550/ARXIV.2207.03764. URL: https://arxiv.org/abs/2207.03764.

[19] Yue Meng et al. "Dark Matter Search Results from the PandaX-4T Commissioning Run". In: *Physical Review Letters* 127.26 (Dec. 2021). DOI: 10.1103/physrevlett.127.261802. URL: https://doi.org/10.1103%2Fphysrevlett.127.261802.

[20] J. Aalbers et al. "DARWIN: towards the ultimate dark matter detector". In: *Journal of Cosmology and Astroparticle Physics* 2016.11 (Nov. 2016), pp. 017–017. DOI: 10.1088/1475-7516/2016/11/017. URL: https://doi.org/10.1088%2F1475-7516%2F2016%2F11%2F017.

[21] Jonathan L. Feng. "Dark Matter Candidates from Particle Physics and Methods of Detection". In: *Annual Review of Astronomy and Astrophysics* 48.1 (Aug. 2010), pp. 495–545. DOI: 10.1146/annurev-astro-082708-101659. URL: https://doi.org/10.1146%2Fannurev-astro-082708-101659.

[22] Ricardo José Mota Peres. *Contributions to the Xenon dark matter experiment*. Coimbra, 2015.

[23] Alison Elliot. "Dark Matter Searches with the ATLAS detector". In: *EPJ Web of Conferences* 158 (Jan. 2017), p. 01007. DOI: 10.1051/epjconf/201715801007.

[24] Adish Vartak. *Dark matter search in CMS. Dark matter searches at the CMS experiment*. Tech. rep. Geneva: CERN, 2017. URL: https://cds.cern.ch/record/2271096.

[25] Julien Billard et al. "Direct detection of dark matter—APPEC committee report∗". In: *Reports on Progress in Physics* 85.5 (Apr. 2022), p. 056201. DOI: 10.1088/1361-6633/ac5754. URL: https://doi.org/10.1088%2F1361-6633%2Fac5754.

[26] Louis E. Strigari. "Galactic searches for dark matter". In: *Physics Reports* 531.1 (Oct. 2013), pp. 1–88. DOI: 10.1016/j.physrep.2013.05.004. URL: https://doi.org/10.1016%5C%2Fj.physrep.2013.05.004.

[27] Louis E. Strigari. "Galactic searches for dark matter". In: *Physics Reports* 531.1 (Oct. 2013), pp. 1–88. DOI: 10.1016/j.physrep.2013.05.004. URL: https://doi.org/10.1016%2Fj.physrep.2013.05.004.

[28] M. Ackermann et al. "Dark matter constraints from observations of 25 Milky Way satellite galaxies with the Fermi Large Area Telescope". In: *Physical Review D* 89.4 (Feb. 2014). DOI: 10.1103/physrevd.89.042001. URL: https://doi.org/10.1103%2Fphysrevd.89.042001.

[29] Miguel Aguilar et al. "The Alpha Magnetic Spectrometer (AMS) on the international space station: Part II — Results from the first seven years". In: *Physics Reports* (2020).

[30] M. G. Aartsen et al. "Search for neutrinos from dark matter self-annihilations in the center of the Milky Way with 3 years of IceCube/DeepCore: IceCube Collaboration". English (US). In: *European Physical Journal C* 77.9 (Sept. 2017). ISSN: 1434-6044. DOI: 10.1140/epjc/s10052-017-5213-y.

[31] C. Amole et al. "Dark matter search results from the PICO-60 $CF_3I$ bubble chamber". In: *Physical Review D* 93.5 (Mar. 2016). DOI: 10.1103/physrevd.93.052014. URL: https://doi.org/10.1103%2Fphysrevd.93.052014.

[32] Elia Bertoldo. "Development of new cryogenic detectors to extend the physics reach of the CRESST experiment". Dec. 2020. URL: http://nbn-resolving.de/urn:nbn:de:bvb:19-273052.

[33] R. Bernabei et al. "The DAMA/LIBRA apparatus". In: *Nuclear Instruments and Methods in Physics Research Section A: Accelerators, Spectrometers, Detectors and Associated Equipment* 592.3 (2008), pp. 297–315. ISSN: 0168-9002. DOI: https://doi.org/10.1016/j.nima.2008.04.082. URL: https://www.sciencedirect.com/science/article/pii/S016890020800675X.

[34] J. Amaré et al. "Annual modulation results from three-year exposure of ANAIS-112". In: *Physical Review D* 103.10 (May 2021). DOI: 10.1103/physrevd.103.102005. URL: https://doi.org/10.1103%2Fphysrevd.103.102005.

[35] E. Aprile and T. Doke. "Liquid xenon detectors for particle physics and astrophysics". In: *Reviews of Modern Physics* 82.3 (July 2010), pp. 2053–2097. DOI: 10.1103/revmodphys.82.2053. URL: https://doi.org/10.1103%2Frevmodphys.82.2053.

[36] E. Aprile et al. "Energy resolution and linearity of XENON1T in the MeV energy range". In: *The European Physical Journal C* 80.8 (Aug. 2020). DOI: 10.1140/epjc/s10052-020-8284-0. URL: https://doi.org/10.1140%2Fepjc%2Fs10052-020-8284-0.

[37] XENON collaboration. *Our Detector: History @ONLINE*. 2022. URL: http://www.xenon1t.org/.

[38] L. Baudis et al. "Design and construction of Xenoscope — a full-scale vertical demonstrator for the DARWIN observatory". In: *Journal of Instrumentation* 16.08 (Aug. 2021), P08052. DOI: 10.1088/1748-0221/16/08/P08052. URL: https://dx.doi.org/10.1088/1748-0221/16/08/P08052.

[39] L. Baudis et al. "Design and construction of Xenoscope — a full-scale vertical demonstrator for the DARWIN observatory". In: *Journal of Instrumentation* 16.08 (Aug. 2021), P08052. DOI: 10.1088/1748-0221/16/08/p08052. URL: https://doi.org/10.1088%2F1748-0221%2F16%2F08%2Fp08052.

[40] F. Arneodo et al. "Cryogenic readout for multiple VUV4 Multi-Pixel Photon Counters in liquid xenon". In: *Nuclear Instruments and Methods in Physics Research Section A: Accelerators, Spectrometers, Detectors and Associated Equipment* 893 (June 2018), pp. 117–123. DOI: 10.1016/j.nima.2018.03.022. URL: https://doi.org/10.1016%2Fj.nima.2018.03.022.

[41] *VUV-MPPC 4th generation (VUV4) Product Flyer*. Hamamatsu Photonics K.K., 2017.

[42] Ardavan Ghassemi, Kota Kobayashi and Kenichi Sato. *A technical guide to silicon photomultipliers (MPPC)*. Hamamatsu Photonics K.K., 2018.

[43] Guido Van Rossum and Fred L. Drake. *Python 3 Reference Manual*. Scotts Valley, CA: CreateSpace, 2009. ISBN: 1441412697.

[44] Jim Pivarski et al. *scikit-hep/uproot5: Version 4.3.7*. Version v4.3.7. Oct. 2022. DOI: 10.5281/zenodo.7157685. URL: https://doi.org/10.5281/zenodo.7157685.

[45] G. Gallina et al. "Characterization of the Hamamatsu VUV4 MPPCs for nEXO". In: *Nuclear Instruments and Methods in Physics Research Section A: Accelerators, Spectrometers, Detectors and Associated Equipment* 940 (Oct. 2019), pp. 371–379. DOI: 10.1016/j.nima.2019.05.096. URL: https://doi.org/10.1016%2Fj.nima.2019.05.096.